Article

Eco-Friendly Synthesis of ZnO Nanoparticles for Quinoline Dye Photodegradation and Antibacterial Applications Using Advanced Machine Learning Models

Hayet Chelghoum [1], Noureddine Nasrallah [2], Hichem Tahraoui [3,4], Mahmoud F. Seleiman [5], Mustapha Mounir Bouhenna [6], Hayet Belmeskine [1], Meriem Zamouche [7], Souhila Djema [6], Jie Zhang [8], Amina Mendil [9], Fayçal Dergal [6], Mohammed Kebir [6,10] and Abdeltif Amrane [4,*]

[1] Department of Biology, Faculty of Nature and Life Sciences, University of Blida, PB270, Soumaa Road, Blida 09000, Algeria; che.hayet@gmail.com (H.C.); hbelmeskine@hotmail.com (H.B.)
[2] Laboratory of Reaction Engineering, Faculty of Mechanical Engineering and Process Engineering, University of Science and Technology Houari Boumediene USTHB, BP 32, Algiers 16111, Algeria; nas_nour@yahoo.fr
[3] Laboratory of Biomaterials and Transport Phenomena, University of Médéa, Médéa 26000, Algeria; hichemm.tahraouii@gmail.com
[4] Ecole Nationale Supérieure de Chimie de Rennes, CNRS, ISCR (Institut des Sciences Chimiques de Rennes) —UMR 6226, University of Rennes, F-35000 Rennes, France
[5] Department of Plant Production, College of Food and Agriculture Sciences, King Saud University, P.O. Box 2460, Riyadh 11451, Saudi Arabia; mseleiman@ksu.edu.sa
[6] Centre de Recherche Scientifique et Technique en Analyses Physico-Chimiques (CRAPC), BP384, Bou-Ismail, Tipaza 42004, Algeria; bouhenna3@yahoo.fr (M.M.B.); djema.souhila@crapc.dz (S.D.); faycal.dergal@gmail.com (F.D.); medkebir@yahoo.fr (M.K.)
[7] Laboratoire de Recherche sur le Médicament et le Développement Durable (ReMeDD), Department of Environmental Engineering, University of Salah Boubnider Constantine 3, El Khroub 25012, Algeria; meriem.zamouche@univ-constantine3.dz
[8] School of Engineering, Merz Court, Newcastle University, Newcastle upon Tyne NE1 7RU, UK; jie.zhang@newcastle.ac.uk
[9] Department of Cellular and Molecular Biology, Faculty of Biological Sciences, "Houari Boumediene" University of Science and Technology, BP 32 El-Alia, Bab Ezzouar, Algiers 16123, Algeria; mendilamina@yahoo.fr
[10] Unité de Recherche en Analyses Physico-Chimiques des Milieux Fluides et Sols—(URAPC-MFS/CRAPC), 11, Chemin Doudou Mokhtar, Ben Aknoun, Alger 16100, Algeria
* Correspondence: abdeltif.amrane@univ-rennes1.fr

Abstract: Community drinking water sources are increasingly contaminated by various point and non-point sources, with emerging organic contaminants and microbial strains posing health risks and disrupting ecosystems. This study explores the use of zinc oxide nanoparticles (ZnO-NPs) as a non-specific agent to address groundwater contamination and combat microbial resistance effectively. The ZnO-NPs were synthesized via a green chemistry approach, employing a sol-gel method with lemon peel aqueous extract. The catalyst was characterized using techniques including XRD, ATR-FTIR, SEM-EDAX, UV-DRS, BET, and Raman spectroscopy. ZnO-NPs were then tested for photodegradation of quinoline yellow dye (QY) under sunlight irradiation, as well as for their antibacterial and antioxidant properties. The ZnO-NP photocatalyst showed significant photoactivity, attributed to effective separation of photogenerated charge carriers. The efficiency of sunlight dye photodegradation was influenced by catalyst dosage (0.1–0.6 mg L^{-1}), pH (3–11), and initial QY concentration (10–50 mg L^{-1}). The study developed a first-order kinetic model for ZnO-NPs using the Langmuir–Hinshelwood equation, yielding kinetic constants of equilibrium adsorption and photodegradation of Kc = 6.632×10^{-2} L mg^{-1} and kH = 7.104×10^{-2} mg L^{-1} min^{-1}, respectively. The results showed that ZnO-NPs were effective against Gram-positive bacterial strains and showed moderate antioxidant activity, suggesting their potential in wastewater disinfection to achieve sustainable development goals. A potential antibacterial mechanism of ZnO-NPs involving interactions with microbial cells is proposed. Additionally, Gaussian Process Regression (GPR) combined with an improved Lévy flight distribution (FDB-LFD) algorithm was used to model QY photodegradation

by ZnO-NPs. The ARD-Exponential kernel function provided high accuracy, validated through residue analysis. Finally, an innovative MATLAB-based application was developed to integrate the GPR_FDB-LFD model and FDB-LFD algorithm, streamlining optimization for precise photodegradation rate predictions. The results obtained in this study show that the GPR and FDB-LFD approaches offer efficient and cost-effective methods for predicting dye photodegradation, saving both time and resources.

---

1. Introduction

Water is the most vulnerable environmental resource and an indispensable element for all life forms. The availability and abundance of water resources have shaped the growth and progress of civilizations. According to the United Nations, one in five inhabitants, or about 30 million people, living in the Mediterranean region lacks access to drinking water [1,2]. As water scarcity becomes a global concern, even developed countries are now experiencing the consequences of excessive irrigation and the challenges posed by a growing population [3].

Pollutants from industrial, agricultural, and urban effluents are often non-biodegradable and persist in the environment [4,5]. Many contribute to water quality degradation, posing significant risks to wildlife and ecosystems. The artificial color known as YQ dye, or E104, is widely utilized in various industries [6,7]. Its ability to dissolve in water allows for its easy dispersion in wastewater, where it can be found as a contaminant in aquatic ecosystems. Its potential health hazards include heightened levels of hyperactivity in children, obsessive-compulsive disorder, male reproductive toxicity, asthma, allergies, tumor formation, and damage to the brain [6,8].

In addition to chemical pollutants, microorganisms from mammalian gut flora and hospital effluents released into the environment can create unfavorable conditions for their host ecosystems [9]; the small-scale discharge of microorganisms leads to an increase in the ambient population as they propagate and proliferate, leading to larger-scale environmental impacts [10,11].

In this context, and given the finite nature of Earth's water resources, effective water treatment is becoming an increasingly pressing issue. Considering the factors at hand, it is worth noting that the existing water treatment methods are quite varied. However, these methods have shown their limitations when treating toxic pollutants. Additionally, some of these methods have drawbacks in specific areas, which highlights the need for new and more efficient treatment systems [12,13].

The search for an alternative or complementary method to conventional methods for wastewater treatment has led to the emergence of new technologies in recent years [14,15]. Among these newer, cleaner technologies to mitigate problems inherent in wastewater treatment, the so-called advanced oxidation processes (AOPs) are of particular interest. These technologies are based on producing non-selective oxidizing reactive species that enable the degradation of many organic pollutants [16,17]. Heterogeneous photocatalysis using nanomaterial catalysts is a promising way of fighting the development of antibacterial and antifungal agents. It is also an improved oxidation technology for wastewater treatment due to its low energy consumption, mild operating conditions, and environmental friendliness [18–21].

However, preparing NPs by various physical and chemical processes remains costly and can be environmentally stressful due to harmful reagents [22,23]. Synthesizing NPs by a biological route constitutes a favorable alternative to chemical and physical methods due to its ecological and economic advantages. This method makes it possible to produce NPs with better physicochemical properties using various bioresources, such as microorganisms and

plant extracts. This practice has garnered considerable interest from researchers worldwide, as biological extract components can reduce metal salts and lead to the formation of metal nanoparticles [24,25].

One such potential source of extract is the fruit of the *Citrus limon* tree, an important medicinal plant belonging to the *Rutaceae* family. The historical utilization of citrus fruits for their therapeutic qualities may be traced back to the 5th and 4th centuries BCE [26]. The *Citrus limon* is known for its rich terpene extracts, particularly D-limonene, α-pinene, α- and β-phellandrene, and sesquiterpene. As terpene chemicals have significant antioxidant properties, they can also act as powerful capping and stabilizing agents for reducing metallic salts to produce oxides in NP form [27].

In recent decades, extensive research has concentrated on diverse methodologies for synthesizing oxides, particularly zinc oxide (ZnO). These investigations seek to enhance the structural, optical, and photocatalytic properties of ZnO, consequently augmenting its efficacy in environmental wastewater treatment, sensors, energy storage, and biological applications.

Optimized ZnO-based materials have proven effective in domains such as the photodegradation of organic molecules, production of structured colors, pharmaceutical products, antibacterial applications, and UV protection. This success has led to sustained interest in new synthesis methods.

In addition, various investigations have been focused on green or chemical ZnO-NP synthesis and their different applications in wastewater treatment or antibacterial disinfection to address challenges, as they offer ample advantages. One study used a green Thymus vulgaris leaf extract to synthesize ZnO nanoparticles for their application as a photocatalyst for degrading the dyes methylene blue (MB), sunfix red (SR) and to treat real textile wastewater (RTW). The study highlighted how ZnO-NPs exhibited a significant degradation efficiency under visible light and achieved degradation rates of 91% for MB and 75% for Sunfix [28].

In recent work addressing clean-up of water pollution, Barleria mysorensis B. Heyne ex Roth was chosen for biosynthesizing ZnO-NPs. The obtained material was tested in the photocatalytic degradation of MB dye. It was revealed that a photodegradation efficiency of approximately 91.32% within 120 min of exposure at a rate constant of 18.34×10^{-3} min^{-1} was achieved, and it was also noted that the dye degradation process followed pseudo-first-order kinetics [29].

In another study, a ZnO-NP was successfully synthesized derived from Crataegus mexicana extract with favorable characteristics for photocatalytic organic dye applications such as methylene blue (MB), malachite green (MG), Congo red (CR), rhodamine b (RB), and methyl orange (MO), demonstrating their potential for the degradation of several organic water contaminants. The results from this study demonstrated that the ZnO-NPs effectively remove all these dyes after 180 min of exposure to light [30]. The microwave-assisted sol-gel process was used to successfully synthesize ZnO-NPs with an average particle size of 24 nm [31]. The structural and morphological characteristics of the nanoparticles were examined, and the photocatalytic degradation of tartrazine dye was analyzed in an aqueous solution under UV-C irradiation to improve the operational settings. Results indicated that 95% of 50 mg L^{-1} of dye was eliminated during 120 min of photocatalytic degradation reaction with 0.02 g of ZnO-NPs [31].

In another study [32], ZnO, SnO$_2$, and their mixed ZnO-SnO$_2$(25%) nanoparticles (NPs) were successfully green synthesized straightforwardly with a low-cost and environmentally friendly approach using a banana peel extract. The degradation efficiency of synthetic dyes ranged from 92.2% to 98%, showcasing the effectiveness of the mixed nanoparticles in dye removal under sunlight. The efficient photocatalytic activity of ZnO-SnO$_2$(25%) NPs is attributed to the effective charge separation and reduced electron/hole recombination rate [32].

Another investigation witnessed the role of green chemistry in the preparation of Zn-NPs via Piper Longum L, showing notable photoreduction rates of 99% for chromium

(VI) and 84% for Sulphanilamide, respectively, in 30–80 min [33]. Additionally, fluconazole was used as a positive control and chloramphenicol was used to test their antibacterial activity against three infections [33].

In one research study [34], an aqueous extract of Myrica esculenta fruit was utilized as a reducing and/or capping agent for the synthesis of ZnO-NPs. The study revealed that ZnO-NPs have high antimicrobial activity against MIC-Bacillus subtilis (0.031 mg/mL), Staphylococcus aureus (0.062 mg/mL), Fusarium oxysporum (0.250 mg/mL), and for *Pseudomonas aeruginosa*, *Escherichia coli*, and *Rosellinia necatrix* (0.125 mg/mL) in comparison to the extract of pure fruits. Additionally, the study also showed strong antioxidant activity (IC50-DPPH: 182.63 $\pm$ 3.21 µg/mL; FRAP: 129.44 µM Ferric sulfate (FeSO$_4$) equivalents). Moreover, the photocatalytic activity demonstrated a 91% photodegradation of methylene blue dye within 180 min [34].

Furthermore, researchers have developed an efficient eco-friendly = method for synthesizing ZnO-NPs utilizing the aqueous extract of Mikaniamicrantha, a terrestrial weed, as a biological reducing agent to convert zinc acetate dehydrate (Zn(CH$_3$COO)$_2$) 2H$_2$O into ZnO-NPs. The produced nanoparticles were evaluated for their antibacterial potential and showed activity against Gram-positive Staphylococcus aureus germs [35].

The aim of another study was to investigate the antibacterial, antioxidant, and photodegradation capabilities of ZnO-NPs produced from the roots of *Taraxacum officinale* radix (dandelion). Due to the ability of ZnO-NPs to generate reactive oxygen species (ROS), which can trigger apoptosis in detrimental cells, it exhibits superior antibacterial efficacy against pathogens such as *Escherichia coli* and Staphylococcus aureus, characterized by a substantial inhibition zone. ZnO-NPs in their produced state generally hold a promising future in wastewater treatment and biomedical applications [36].

In [37], an as-prepared ZnO-SnO$_2$ nanocomposite by sol-gel method was characterized by X-ray diffraction (XRD), scanning electron micrography (SEM-EDX), FTIR, and UV-visible spectrometer analysis techniques. The obtained nanocomposite exhibited an average particle size of 22 nm and a bandgap of 5.06 eV. Moreover, the ZnO-SnO$_2$ nanocomposite was used in varying concentrations as an antibacterial and antifungal against *Salmonella typhias*, *Listeria monocytogenes*, *Staph aureus*, and *E. coli*, as well as against Candida albicans and Aspergillus niger fungus. The study indicated that ZnO-SnO$_2$ nanocomposite exhibits effective antibacterial activity against both Gram-positive and Gram-negative bacteria, as demonstrated through turbidity and inhibition zone methods. Moreover, antifungal activity was observed against various pathogens [37].

The objectives of the present study include the eco-friendly synthesis of ZnO nanoparticles, evaluation of their photocatalytic and antibacterial activities, and optimization of photodegradation activity by Gaussian Process Regression. We report, for the first time, employing a hydro-distillation of *Citrus limon* peel extract as a mediator in the synthesis of ZnO-NPs to facilitate and promote environmental sustainability. Firstly, this environmentally beneficial method makes use of the hydro-distillation extract's natural bioactive components, which function as stabilizing and reducing agents and help in the production of ZnO-NPs. Secondly, these NPs underwent detailed characterization using various techniques such as TGA, XRD, ATR-FTIR, SEM-EDAX, UV-DRS, BET, and Raman spectroscopy analyses. Thirdly, their effectiveness and performance in the photocatalytic degradation of the QY dye were assessed under direct sun radiation exposure. Moreover, the modelling of photodegradation kinetics was performed using the Langmuir–Hinshelwood model, while their antibacterial efficiency was evaluated against five bacterial strains, and their antioxidant potential was measured. Innovatively, the modeling of QY dye degradation by ZnO-NPs was carried out using GPR with the FDB-LFD algorithm [38]. The developed model was then employed to determine the optimal conditions that could lead to more effective environmental dye degradation using the same FDB-LFD algorithm, and its predictions were validated through laboratory experiments. The integration of GPR with the FDB-LFD algorithm sets new standards in modeling dye degradation processes. Importantly, this study marks the first application of this methodology in this specific

context, making it a pioneering contribution to research in nanotechnology and dye degradation. Furthermore, an innovative MATLAB application was created to streamline the optimization of dye degradation conditions, providing a valuable tool for environmental researchers and practitioners.

2. Results and Discussion

2.1. Thermal Properties of ZnO-NPs

The analysis was carried out at high temperatures using thermogravimetric analysis (TGA) and differential thermal analysis (DTA) under a nitrogen atmosphere to study the thermal stability of ZnO. The obtained results are depicted in Figure 1, which shows that a preliminary reduction in mass of 10% was observed in the temperature range of 25 to 150 °C, which may be attributed to the evaporation of water molecules as a consequence of the moisture removal. A further additional weight loss of up to 44% can be attributed to emissions of carbon dioxide and carbon monoxide in their gaseous state, released during the decomposition of the plant extracts and organic compounds. However, a plateau is observed in the temperature range up to 400 °C, indicating that 500 °C is the optimal temperature to obtain the desired pure phase of zinc oxide [39]. On the other hand, we observed the presence of two endothermic peaks in the differential thermal analysis (DTA) curve, occurring at temperatures of 80 °C and 410 °C, providing evidence of a two-stage decomposition process of the precursor and biomolecule reactants acting as reducing agents [40].
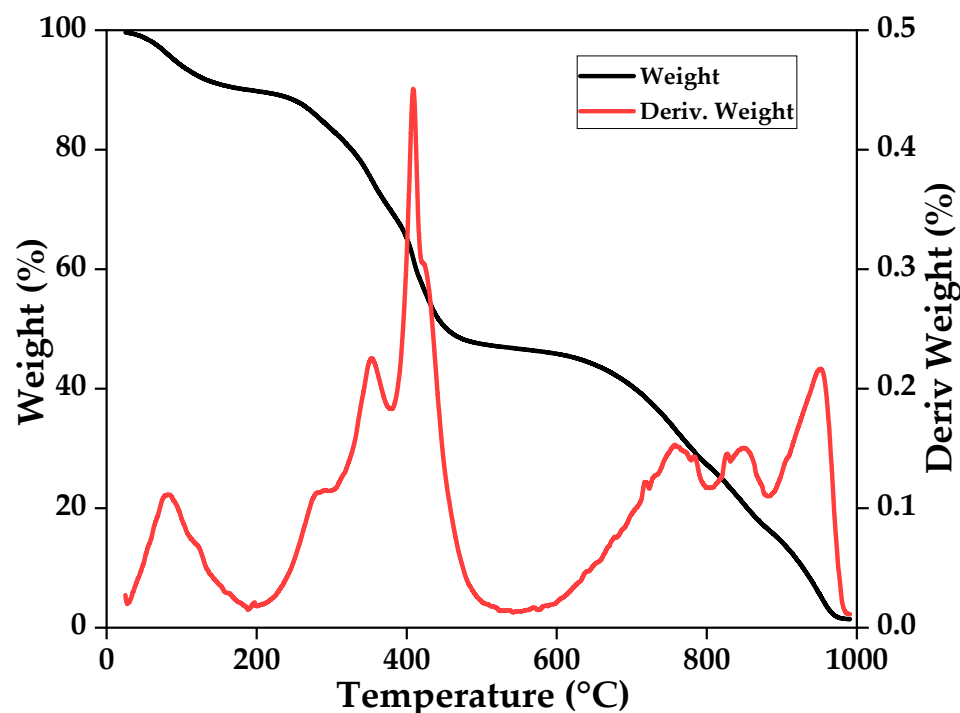

Figure 1. TGA and DTA plot of the reagent's mixture used for ZnO under N_2 environment.

2.2. Structural Properties

X-ray diffraction analysis was conducted using a Bruker D8 Advance diffractometer, using the copper Kα line with a wavelength of λ = 1.5406 Å. The XRD pattern of ZnO, presented in Figure 2 across an angular range of 2θ from 5 to 80°, shows that the synthesized compound exhibits diffraction peaks at 31.37°, 34.37°, 36.21°, 47.52°, 56.56°, 62.84°, 67.91°, and 69.06°. These peaks correspond to the indexed (100), (002), (101), (102), (110), (103), (112), and (201) planes, according to the JDCP card No (36–1451) [41,42], confirming a (P63mc) crystalline hexagonal structure with lattice parameters a = b = 3.2488 Å and c = 5.2054 Å. After comparing the diffraction angles with those reported on the JDCP card

(36–1451), the intense and symmetrical lines indicate the compound's high crystallinity. In addition, the width at half height of the X-ray diffraction peaks is relatively wide, suggesting that the crystallite size of ZnO is in the nanometer range [43,44].
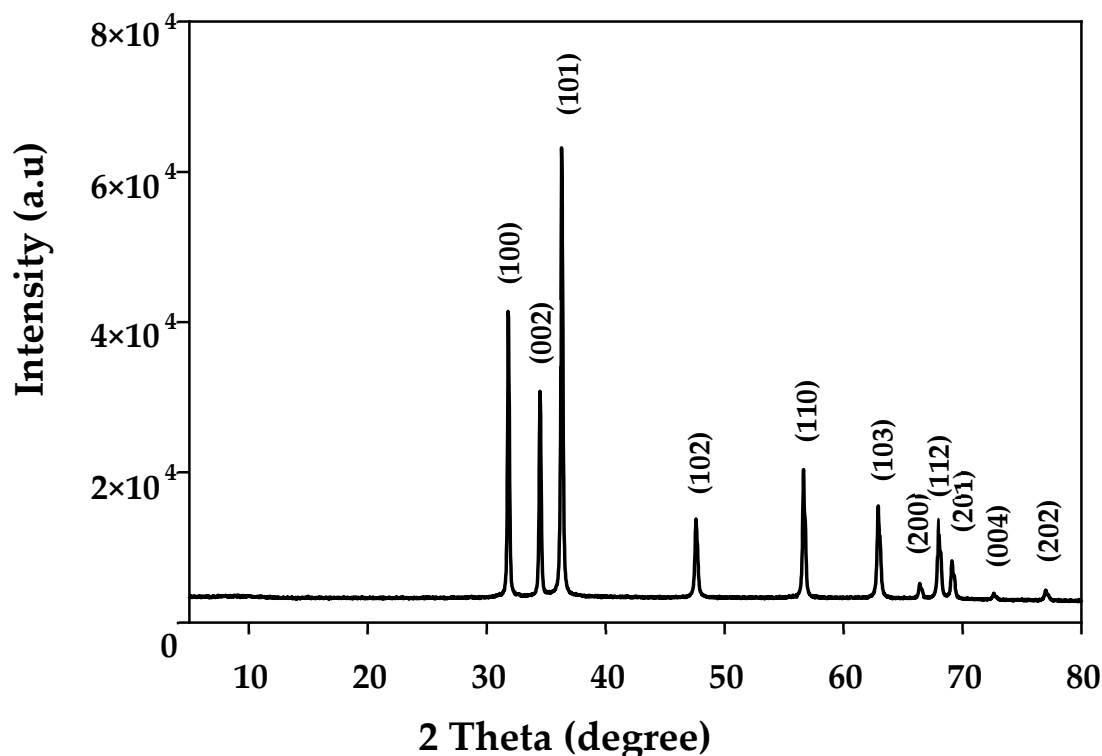

Figure 2. XRD patterns of ZnO-NPs synthesized by sol-gel mediated green chemistry.

These results confirm that the ZnO-NPs synthesized using a modified sol-gel method with green chemistry possess well-defined crystal morphology and that the planes are in accordance with the würtzite structure (hexagonal structure). The different values of particle diameter d and lattice parameters of ZnO-NPs were estimated [a = b = 3.2488 Å and c = 5.2054 Å] according to JCPDS No 01–089-0510. The calculated average crystallite size of ZnO-NPs was 22.10 nm, according to the FWHM formula. The significantly broad diffraction plane width indicates the formation of very small crystalline NPs.

To obtain more detailed information about the crystallite structure, phonon, modes, defects, and strains, Raman spectroscopy was used to analyze the characteristic vibrational lines of the studied sample. Table 1 shows the main vibrational modes observed in the synthesized ZnO of würtzite-type structure. ZnO observed for the synthesized ZnO.

Table 1. Frequencies of various Raman bands of prepared ZnO.

Sample	Frequency (cm^{-1})	Vibration Mode
	100	E2
	240	B1
	422	E1(TO)
ZnO (würtzite)	437	E2
	540	B1
	575	E1(LO)
	686	A1(LO)

For the prepared ZnO, the presence of lines at 100 cm^{-1} and 437 cm^{-1} of vibration mode E2 are characteristic of the würtzite structure [45]. This is explained by the decrease in the size of the crystallites, which leads, at the same time, to a shift of some cm^{-1} towards the higher energies of the Eg vibration, as well as a widening of this line. The dimensional confinement seems to be at the origin of this phenomenon [46]. This shift is also observed for the nanostructured ZnO material.

The Raman spectra of the ZnO-NP powder are provided by Figure 3, which revealed the presence of the following distinct peaks located at 99, 334, 436, and 686 cm^{-1}. Raman shifts correspond to the eigenmodes of E_2(low), E_2(high)-E_2(low) modes, E_2(high), and A_1(LO), respectively [45,47]. The value of the peak at 686 cm^{-1} is attributed to the A1(LO) mode, which corresponds to longitudinal optical phonons. It is essential to understand this mode in order to understand electronic transitions and the effects of factors such as doping and particle size.
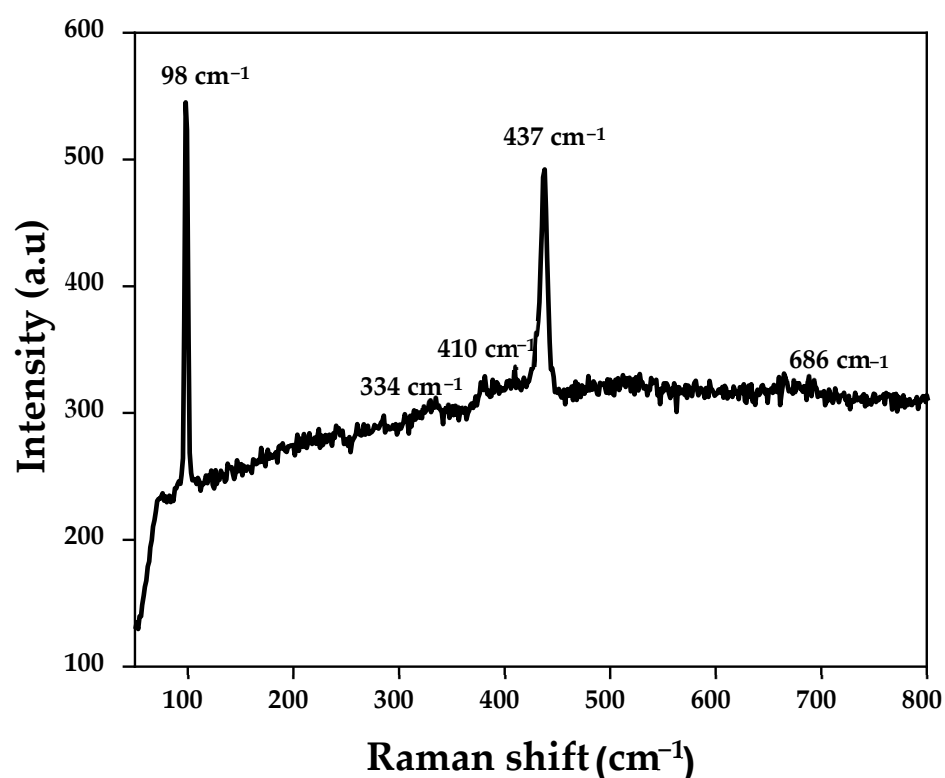

Figure 3. Room temperature Raman spectra of ZnO (bottom) powders.

Furthermore, Raman spectra of this ZnO synthesized sample show a hump-like characteristic vibration peak associated with an oxygen vacancy (Vo) defect; although very weak in intensity, in the range of 510 cm^{-1} to 700 cm^{-1}, it wholly overlapped with the eigenmode of A1(LO) [48].

2.3. ZnO-NP Morphology and Size Distribution

To illustrate the nanometric structure of our ZnO-NPs, scanning electron microscopy analysis was conducted on a sol-gel-synthesized ZnO sample modified using a green chemistry method. Figure 4a shows a well-crystallized powder consisting of ZnO particles with spherical or pseudo-spherical morphologies. The formation of more significant nanoparticles may potentially lead to the blockage of holes due to the potential aggregation phenomenon [49–51]; this indicates that the powder presents a morphology constituted of irregular spherical shapes with large agglomerations between them, which is most likely due to the high surface area of the ZnO-NPs [42]. A histogram of the particle size distribution determined from the SEM images using ImageJ plugin (1.8.0_172) development

software revealed that these aggregates comprise nanoparticles with a size of 77.95 nm (Figure 4b), clearly confirming the nanometric nature of our ZnO-NPs. This is consistent with previously reported results [52]. Furthermore, the ZnO-NPs demonstrated a low BET surface area of 12.35 m^2/g, suggesting a mesoporous structure. This value is comparatively low against values for ZnO synthesized and documented elsewhere in the literature [53].

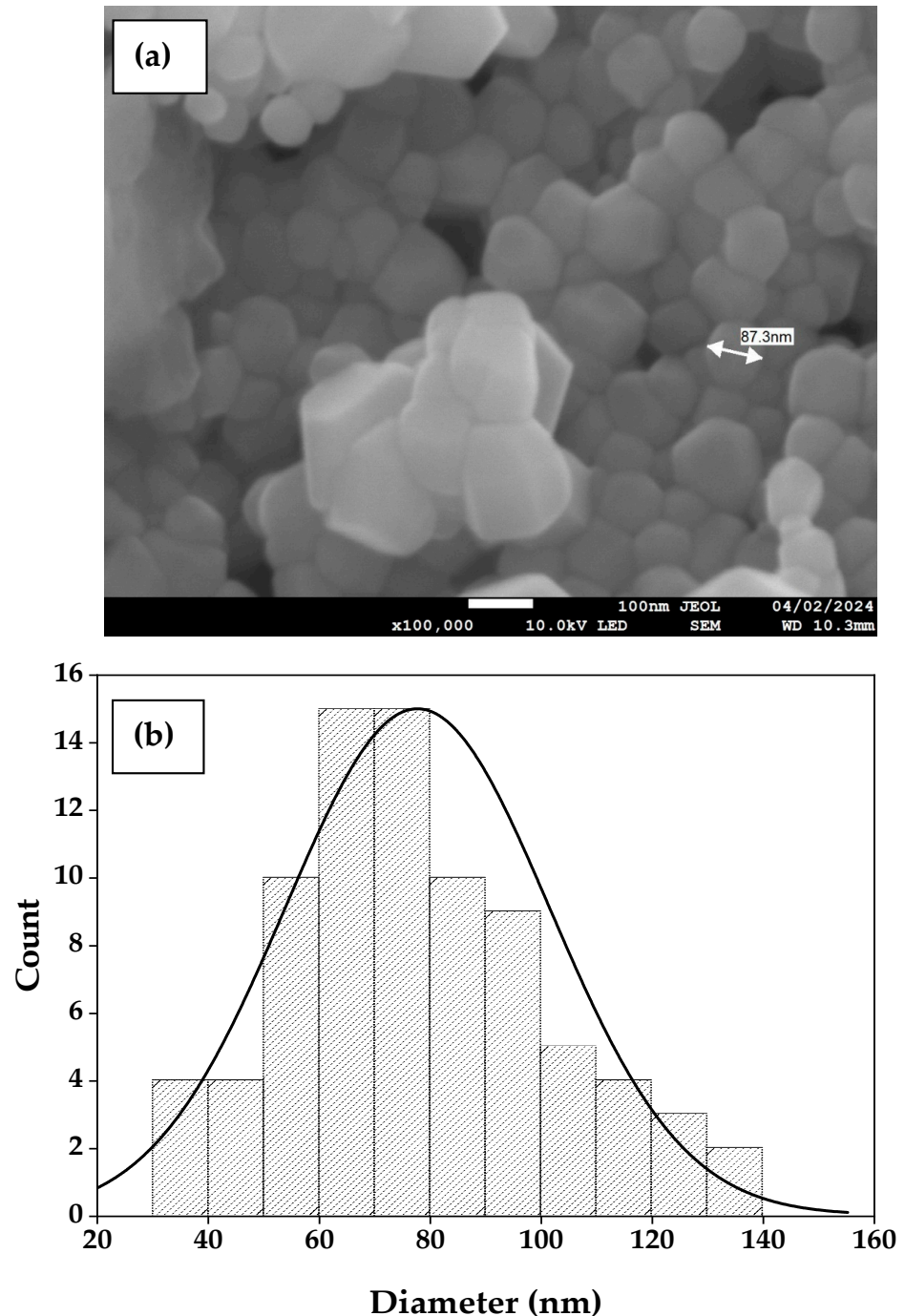**Figure 4.** SEM analysis (**a**) and particle size distribution (**b**) of the prepared ZnO-NPs.

2.4. Chemical Composition and Surface Properties

The ZnO-NP chemical composition can be confirmed by elemental analysis using EDS, as illustrated in Figure 5.
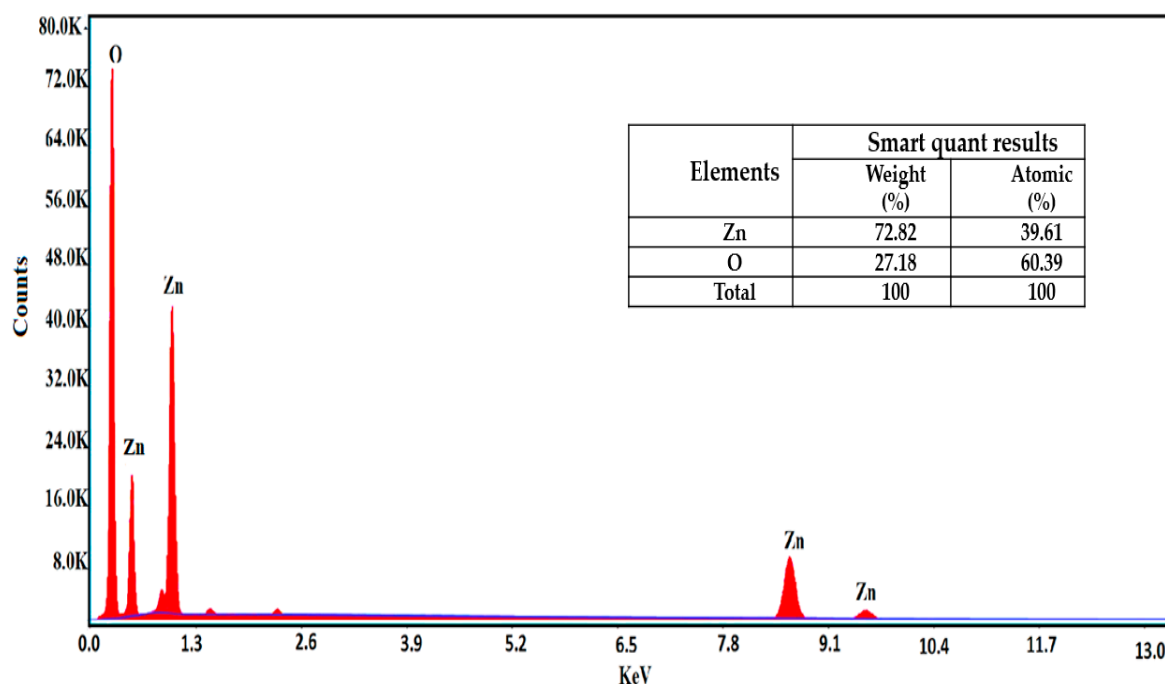
Figure 5. EDS spectra of ZnO-NPs.

The EDS spectra clearly show prominent peaks for Zn and O, with a minor trace of carbon (C), indicating weight percentages of approximately 72.82% zinc and 27.18% oxygen. This analysis highlights the predominance of zinc and oxygen in the sample, consistent with results reported by Ahmad et al., who observed a ZnO composition of 79.35% zinc and 20.65% oxygen by weight [54]. According to these spectra, no significant characteristic peaks of any other impurities were observed, indicating the formation of a pure ZnO material [55].

For a deeper understanding of the surface properties of ZnO-NPs, the zeta potential measurement is performed to detect the surface charges acquired by the NPs, to provide information on particle stability and determine whether electrostatic repulsions are capable of maintaining the dispersion of particle powder. The zeta potential of the prepared ZnO-NPs was found to be −53.8 mV (Figure S1). The negative value indicates the presence of repulsion between the ZnO particles in an aqueous solution, which enhances stability and prevents their aggregation [56].

ATR-FTIR analysis is a widely used technique for identifying the functional groups found on the NP's surface. This method offers insights into the chemical bonds and molecular vibrations found in ZnO-NPs. Figure 6 shows the ATR-FTIR spectra generated by the ZnO sample in the 400 to 4000 cm^{-1} spectral range. It shows that the ATR-FTIR spectra of ZnO-NPs exhibit many distinct peaks at 407 cm^{-1}, 430 cm^{-1}, 594 cm^{-1}, 782 cm^{-1}, 1096 cm^{-1}, 1334 cm^{-1}, 1572 cm^{-1}, 1976 cm^{-1}, 2046 cm^{-1}, 2277 cm^{-1}, and 3324 cm^{-1}, indicating the presence of several chemical components in citron lemon, such as alkaloids, glycosides, flavonoids, and steroids, which may explain the reported number of functional groups [57]. These chemicals have been identified as having reducing and capping characteristics. It was discovered that the sharp peak positioned at 430 cm^{-1} may be ascribed to ZnO stretching bonds [58,59]. Nevertheless, the bands shown in Figure 6 are situated inside the designated 600–1700 cm^{-1} region and correspond to the functional groups C=O, C–O, and C–H, respectively [41,60]. Another broad peak at 3324 cm^{-1} may be due to the O–H stretching vibrations and bending modes of the adsorbed water [61].
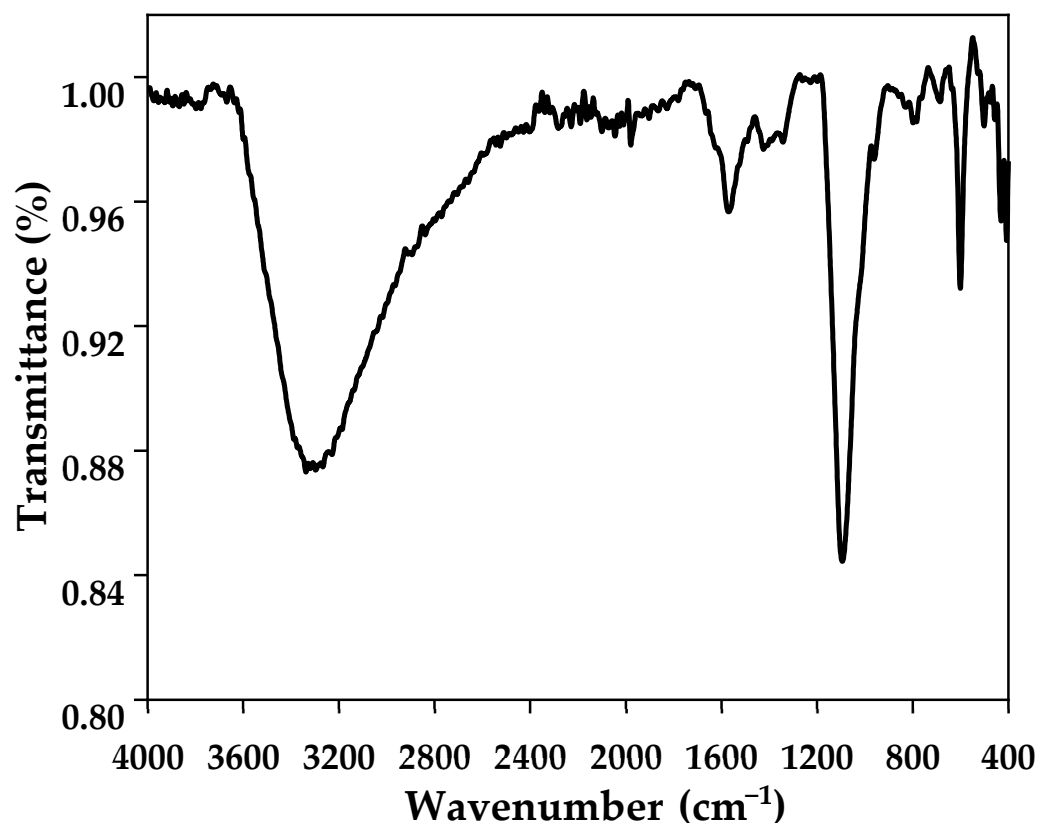
Figure 6. ATR-FTIR spectra of ZnO-NPs.

2.5. Optical Properties of ZnO-NPs

UV-visible spectrophotometry absorption is an optical method used to characterize substances that can be applied to investigate the ZnO-NPs bandgap energy. As can be seen from Figure 7a, the absorbance spectra of ZnO-NPs correspond to the wavelengths. The absorption band edge of ZnO was observed at 350 nm. However, the optical bandgap (Eg) of ZnO was calculated from the plot of $(\alpha h\nu)^2$ versus $h\nu$ (Figure 7b) by using the Tauc's relation given by Equation (1) [62]:

$$(\alpha h\nu)^n = c(h\nu - Eg) \tag{1}$$

where $h\nu$ is the photon energy, α is the absorption coefficient, c is constant relative to the material, and n is the parameter associated with the different types of electronic transitions.

The obtained data revealed that ZnO-NPs is a direct gap oxide. Thus, the value of n has been chosen to be 2. To calculate the ZnO-NPs Eg value, the linear portion of the $(\alpha h\nu)^2$ was extrapolated to the $h\nu = 0$ (Figure 7b). An excitonic absorption peak is found at about 350 nm due to the ZnO-NPs being well below the bandgap wavelength of 350 nm (Eg = 3.2 eV). On the other hand, it is evident that the significant net absorption of ZnO indicates the monodisperse nature of the nanoparticle distribution [63,64] and exciton recombination, which means a lower particle size for ZnO-NPs [65]. Additionally, the agglomeration of particles and the presence of impurities such as residual carbon [66] and the high annealing temperatures for the production of ZnO [67] can also account for the low values of the Eg obtained.
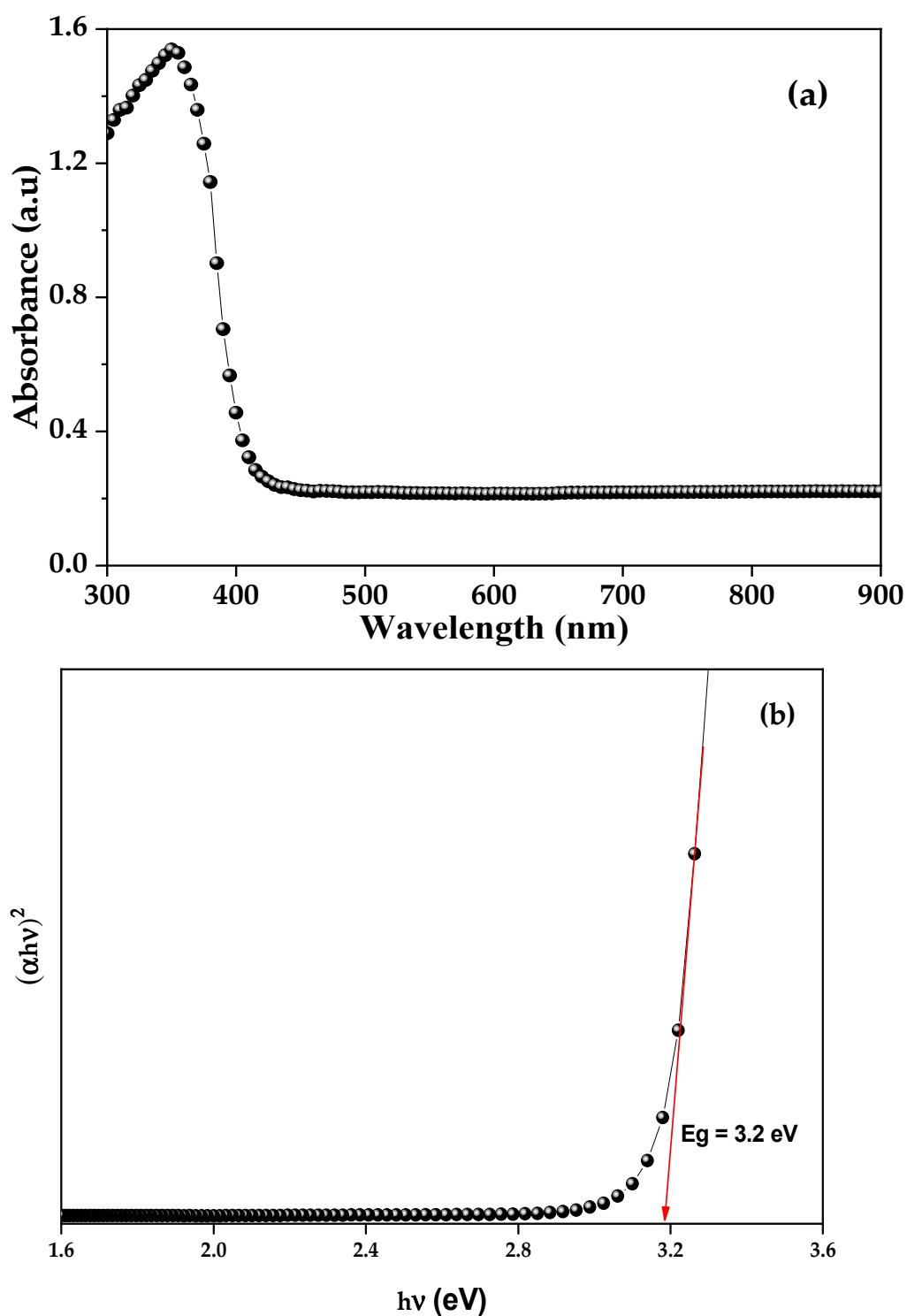
Figure 7. UV-visible diffuse reflectance spectra (**a**); the Tauc-plot variation of (αhν)² versus photon energy of ZnO-NPs (**b**).

2.6. Photocatalytic Performance of ZnO-NPs

The performance of the synthesized ZnO-NPs was evaluated for the removal of QY dye from an aqueous solution via photodegradation under natural sunlight irradiation. This experiment was conducted in July 2019 between 10:00 and 14:00 at the University of Science and Technology Houari Boumediene (USTHB), located in Bab Ezzouar, in the northcentral part of Algeria (latitude 36.716835 and longitude 3.1805583). The study examined the effects

of various factors on the photodegradation efficiency, including the amount of ZnO-NP catalyst, the pH of the medium, and the initial QY dye concentration.

2.6.1. Effect of Catalyst Dose

Generally, the photodegradation efficiency for removing pollutant molecules in an aqueous solution is directly proportional to the amount of the catalyst. Increasing the available surface of oxide for the adsorption of irradiation photons can thus enhance the dye's photodegradation reaction [68]. To optimize the required mass of ZnO-NPs, a series of experiments were conducted by varying the amount of the ZnO from 0.1 to 0.6 g L^{-1} for an initial QY dye concentration of 10 mg L^{-1} under sunlight exposure. During the reaction, the suspension mixture was stirred to prevent ZnO-NPs from settling, ensuring thorough homogenization. Samples were taken at regular intervals (up to 4 h) and the aliquots were centrifuged to separate the catalyst. The QY removal efficiency was determined spectrophotometrically based on the absorption at a wavelength of 414 nm. The absorbance value was then converted to concentration value via the standard calibration curve. The obtained results are shown in Figure 8a.

As shown in Figure 8a, the photocatalytic performance improves with an increase in the quantity of ZnO-NPs, leading to a higher efficiency in QY dye removal. This improvement can be attributed to the availability of more binding sites for QY adsorption, as well as the increase in electron-hole pairs on the catalyst surface [69].

Furthermore, the photodegradation yields increased from 68% to 98% when the mass of ZnO was increased from 0.1 g to 0.6 g. Based on the results, a ZnO mass of 0.3 g is considered optimal. Beyond this amount, the reaction becomes independent of the catalyst dose, likely due to the phenomenon of scaling effect. The stagnation of the photocatalytic activity of ZnO at this value is attributed to the saturation of the photon absorbance of ZnO. However, the aggregation of ZnO particles, which is favored by high concentrations, may also contribute to a decrease in photocatalytic activity [70].

Figure 8. *Cont.*
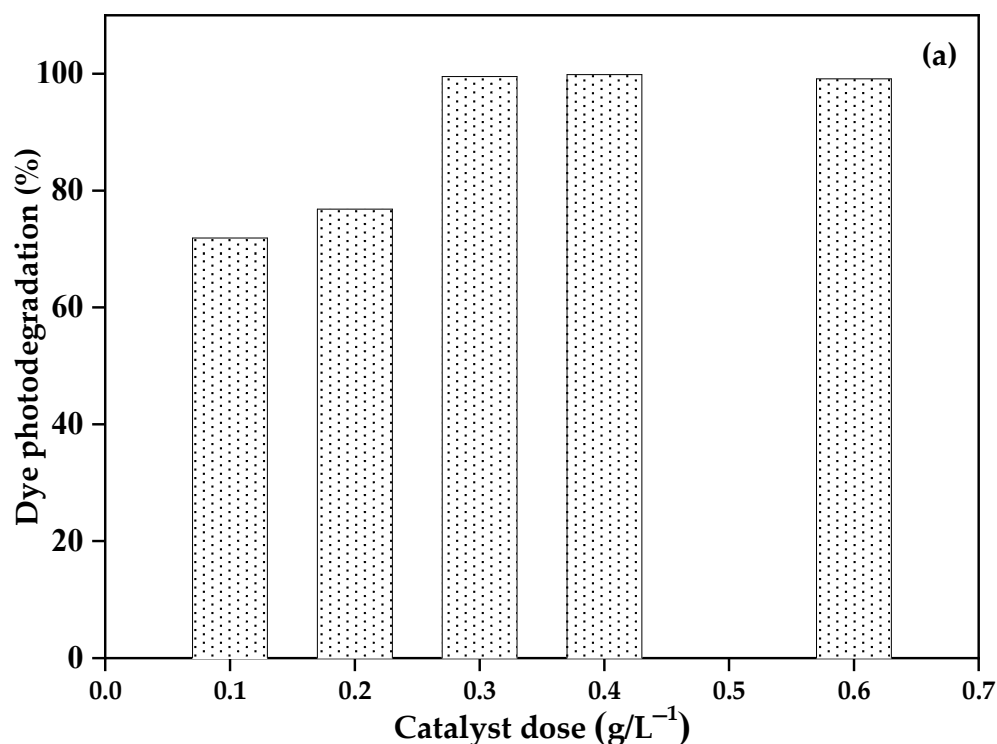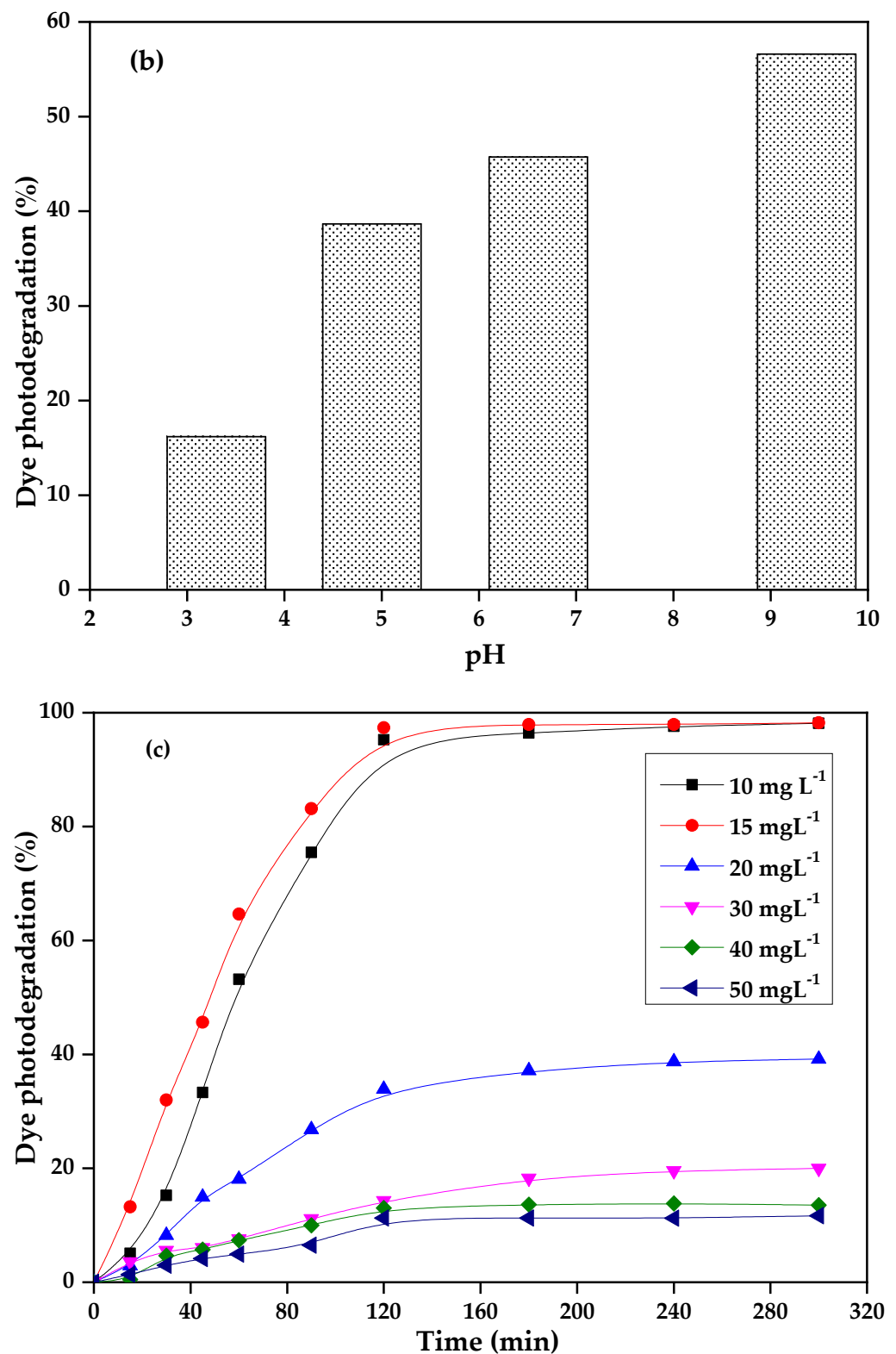
Figure 8. Progression of QY removal efficiency via photodegradation, as a function of different (**a**) ZnO-NP masses, (**b**) pH, (**c**) initial dye concentrations. (Experimental conditions: catalyst dose = 0.3 g L^{-1}, pH = 9, 25 °C.)

2.6.2. Effect of pH on the Rate of QY Removal

The pH level of the medium is widely regarded in the literature as one of the most influential factors in the photodegradation process, as it affects the charge distribution on the surface of the catalyst powder. Moreover, industrial wastewater often contains dyes at varying pH levels, making it essential to study the impact of pH on dye photodegradation [71].

To investigate the influence of pH on QY photodegradation in the presence of ZnO-NPs under sunlight, a series of experiments was conducted. A 100 mL solution of QY (20 mg L^{-1}) was reacted with 0.1 g L^{-1} of ZnO catalyst powder, with pH values adjusted between 3 and 9 by adding precise amounts of 0.1 mol L^{-1} HCl or sodium NaOH solution. The final pH values were measured with a pH meter. The reaction took place at room temperature under sunlight, with samples collected at regular intervals for analysis using a Shimadzu 1800 UV-vis spectrophotometer. Figure 8b illustrates the progression of QY photodegradation efficiency over time across the various pH levels.

As shown in Figure 8b, QY photodegradation efficiency is significantly higher in a basic medium (pH = 9), with the elimination rate increasing as pH rises. In contrast, the low rates of photodegradation recorded in the acidic medium are due to the dissolution of the catalyst, i.e., it can change the photocatalytic characteristics of the semiconductor [72], the electrical charge of the particles, the size of the aggregates formed, the position of the conduction and valence bands of the semiconductor catalysts, and the degree of adsorption of the electron donors on the catalyst surface.

Since the negative value of the zeta potential is anticipated, the adsorption of QY on the surface of the ZnO-NPs is expected to be enhanced in the basic medium. Photogenerated holes can either directly oxidize the dye into reactive intermediates or react with hydroxyl ions (OH^{-}), resulting in the creation of highly reactive hydroxyl radicals that further complete mineralization of the dye [73].

2.6.3. Effect of Initial Concentration of QY

Due to the high impact of its initial concentration on the kinetic rate and efficiency of the photodegradation process, several authors have investigated the effect of varying the initial pollutant concentration on photocatalytic processes [74,75]. These authors have reported that the rate of kinetic photodegradation of organic compounds increases with increasing initial concentration, up to a certain concentration level. Above this level, increasing concentration leads to a decrease in the photodegradation rate. During dye adsorption, a thermodynamic equilibrium between the liquid solution and solid phase of the photocatalyst is reached, where the adsorbed quantity of the dye is a function of the initial concentration of the pollutant in the effluent [76].

The study of the initial dye concentration effect was conducted under sunlight irradiation, with a series of standard solutions of QY dye with concentrations ranging from 10 to 50 mg L^{-1}, with an adjusted medium pH of 9 and a catalyst dosage of 0.3 g L^{-1}. A duration of 5 h was established to study the effect of the initial dye concentration on the photocatalytic process under sunlight (Figure 8c). Figure 8c shows the efficiency of photodegradation of different initial concentrations of QY as a function of time.

Increasing the initial concentration of the QY dye induces the formation of aggregation as a screen layer on the photocatalyst surface. As a result, an insufficient quantity of energy photons can penetrate the photocatalyst surface to promote redox reactions, thus limiting the generation of reactive species and consequently reducing the photocatalytic degradation of the dye [77]. Moreover, an increase in dye concentration leads to enhanced light absorption by the dye molecules, which may result in diminished light penetration to the photocatalyst surface, hence further decreasing photodegradation efficiency [78].

Figure 8c illustrates the photodegradation kinetics of the QY dye as a function of irradiation time in the presence of ZnO. The data reveal a clear correlation between the initial dye concentration and photodegradation effectiveness [79]. Specifically, higher initial concentrations of dye exhibit a gradual slowing of the degradation rate, requiring

longer irradiation times for complete removal compared to lower concentrations [80]. For instance, at a dye concentration of 10 mg L^{-1}, complete photodegradation has occurred at 120 min, whereas a concentration of 50 mg L^{-1} necessitates 240 min of irradiation for complete elimination.

2.6.4. Kinetic Study of Photocatalysis

In the photodegradation process, it is admitted that several reactions take place on the surface of the catalyst. However, estimating the proportion of substrate adsorption on the catalyst can provide helpful information for studying the pollutant photodegradation kinetics [81].

To describe the order of the QY photodegradation reaction, a simplified first-order model can be represented by the Langmuir–Hinshelwood model, which is described by the following equation [82]:

$$V = -\frac{dc}{dt} = K_{app}\, C_t \tag{2}$$

where V is the photodegradation rate (mg L^{-1} min^{-1}), K$_{app}$ is the apparent constant (min^{-1}), C$_t$ is the pollutant concentration, and t is the irradiation time (min).

The integration of this equation using the limitation conditions (C = Co when t = 0) results in the following equation:

$$\ln\left(\frac{C_o}{C_t}\right) = K_{app}\, t \tag{3}$$

The plot of ln(C$_o$/C$_t$) as a function of time at different concentrations gives straight lines with slopes equal to K$_{app}$, as shown in Figure 9.
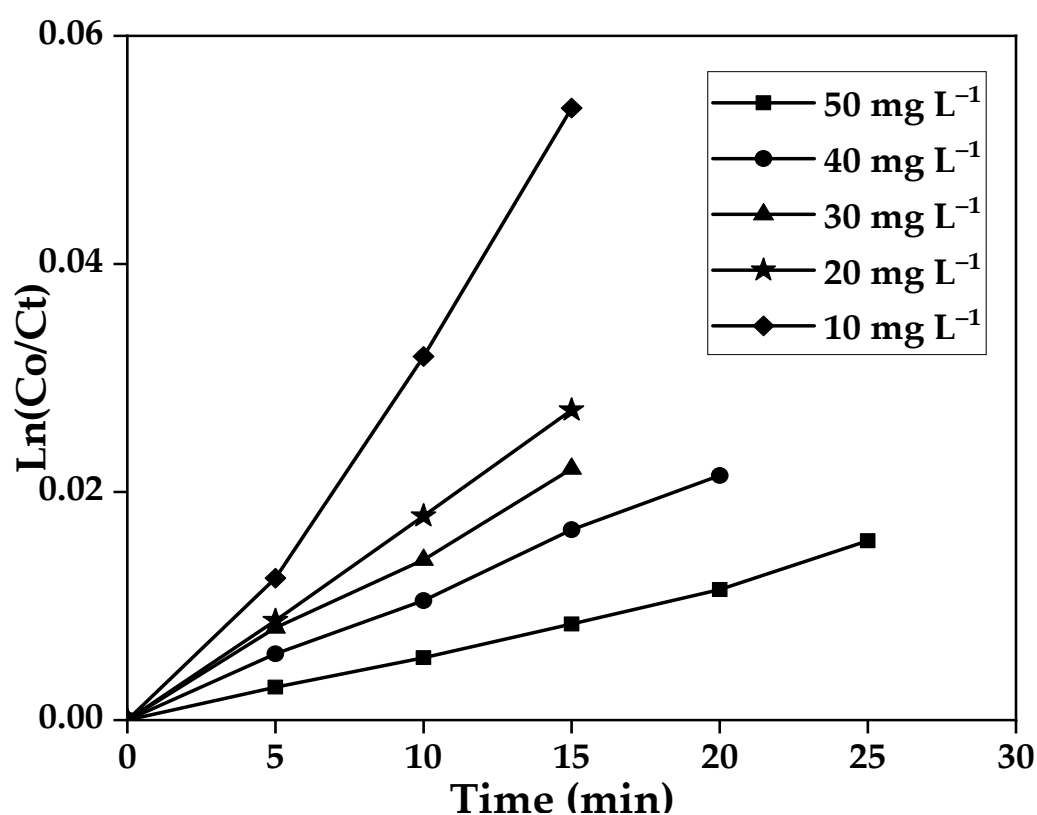

Figure 9. Kinetics of photodegradation of different initial concentrations of QY dye.

The plot of $1/K_{app}$ as a function of the initial QY dye concentration allows us to determine the constants K_H and K_C from the equation [83]:

$$\frac{1}{K_{app}} = \frac{1}{K_H K_C} + \frac{C_o}{K_C} \tag{4}$$

where K_H is a constant that depends on other factors influencing the process (mg L^{-1} min^{-1}) and K_C is the equilibrium adsorption constant (L mg^{-1}).

By fitting the $(1/K_{app})$ vs. (C_o), the values of the adsorption equilibrium and photodegradation constants (K_H) and the second-order constant (K_C) were obtained. These are shown in Table 2.

Table 2. Kinetic parameters of photocatalysis for different concentrations.

C (mg L^{-1})	K_{app} (min^{-1})	$t_{1/2}$ (min)	R^2	K_C (L mg^{-1})	K_H (mg L^{-1} min^{-1})	θ
10	0.0036	192.54	0.9417			3.587×10^{-3}
20	0.0017	407.73	0.9921			1.697×10^{-3}
30	0.0014	495.105	0.9884	6.632×10^{-2}	7.104×10^{-2}	1.398×10^{-3}
40	0.0012	577.62	0.9971			1.198×10^{-3}
50	0.0011	630.13	0.9457			1.098×10^{-3}

The kinetic study allowed us to estimate the half-life $(t_{1/2})$ of the photodegradation of QY employing the following equation [84]:

$$t_{\frac{1}{2}} = \frac{\ln 2}{K_{app}} \tag{5}$$

The parameter θ is the coverage rate of the catalyst surface or occupancy of the catalyst active sites by reactants, expressed in Equation (6) [85]:

$$\theta = \frac{K_c C_{ads}}{1 + K_c C_{ads}} \tag{6}$$

where K_c and C_{ads} represent the equilibrium adsorption constant and adsorption concentration, respectively.

Based on the results of Table 2, the values obtained for each concentration, the Langmuir–Hinshelwood model is confirmed in the photodegradation of QY dye.

It can be observed from Table 2 that the values of K_{app} reduce with the rise in initial QY concentration. Conversely, the half-life time $t_{1/2}$ increases with increasing initial QY concentration. This behavior is due to the high number of QY molecules in the solution, which can lead to self-screening effects. Also, the decrease of the coverage rate θ of the ZnO-NPs surface is due to the tendency of QY molecules to aggregate and form a dense layer or screen over the catalyst active sites [86].

The kinetic constants of equilibrium adsorption Kc and photodegradation K_H are 6.632×10^{-2} L mg^{-1} and 7.104×10^{-2} mg L^{-1} min^{-1}, respectively, determined by linear regression of the plot $1/K_{app}$ vs. Co (Figure 10). These are of the same order of magnitude as those reported in the literature for the photodegradation of antibiotics [87]. These findings support the suitability of the LH model to describe the kinetics of QY degradation under the investigated conditions.
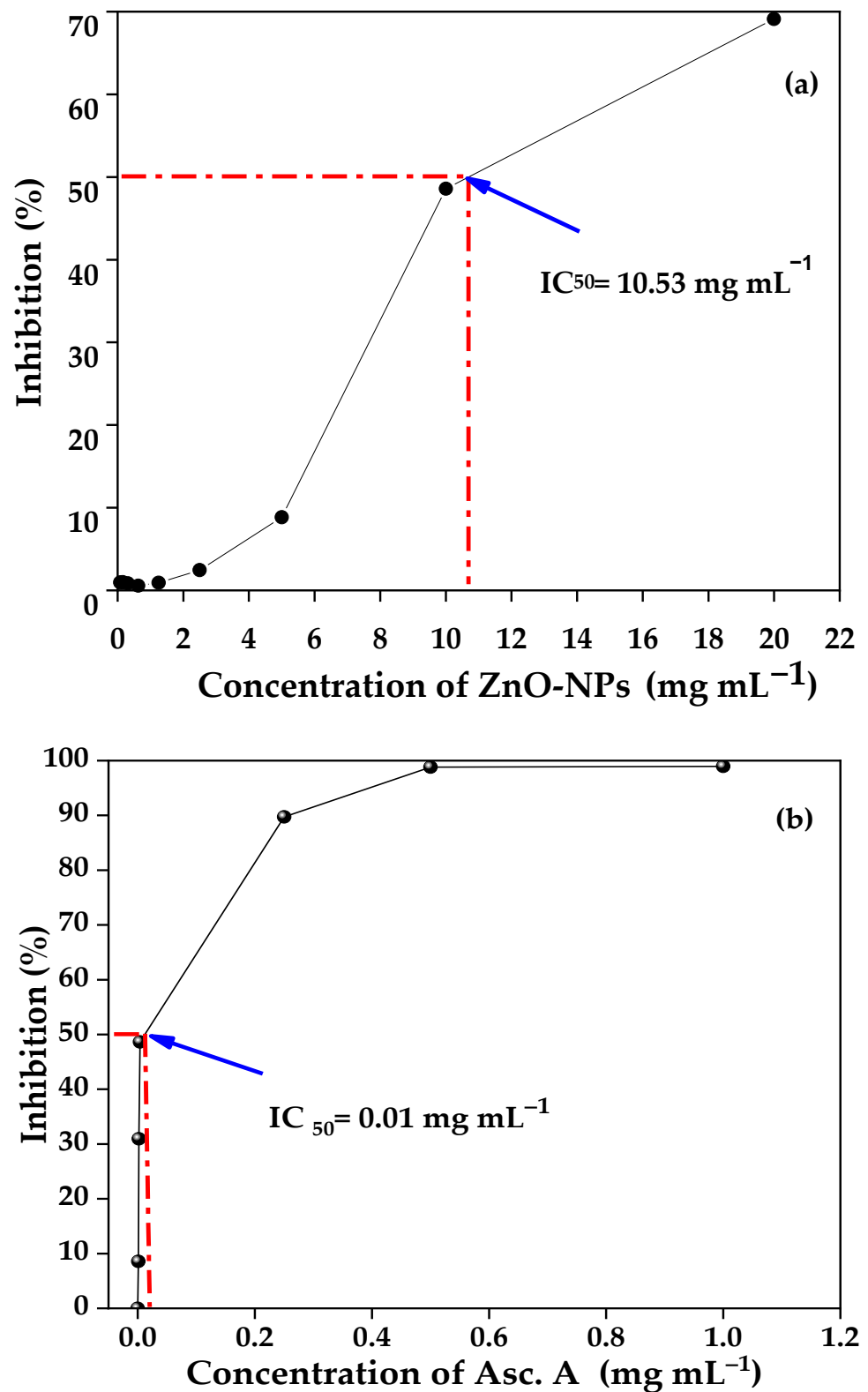
Figure 10. DPPH radical scavenging activity of (**a**) prepared ZnO-NPs and (**b**) ascorbic acid.

2.7. Antioxidant Activity

The antioxidant properties of the produced ZnO were evaluated using the DPPH technique. ZnO-NP solutions with concentrations ranging from 0 to 20 mg mL^{-1} reacted with 0.1 mM of DPPH. The antioxidant scavenging potential is indicated according to

the degree of discoloration. Using a UV-vis spectrophotometer, each sample's absorbance values were measured against the DPPH radical at 517 nm. Figure 10 displays the change in the inhibition percentage (I%) as a function of the different concentrations of ZnO-NPs (Figure 10a) and the standard antioxidant (ascorbic acid) (Figure 10b), as well as the IC50 values.

According to the results displayed in Figure 10a, it can be seen that the ZnO showed moderate antioxidant activity. The activity was observed to be influenced by the concentration of ZnO. Additionally, it can be observed that, as the concentration increased, the percentage of inhibition also increased. The highest concentrations revealed the most prominent antioxidant properties of ZnO-NPs. When the concentration of ZnO-NPs was 20 mg ml^{-1}, it was shown that they had an inhibitory rate of 69.11%, as depicted in Figure 10a. However, a lower inhibition level was shown compared to that observed in the positive control (ascorbic acid). Our findings line up with the ZnO-NPs biosynthesized antioxidant activity using various plant extracts: *Azadirachta indica*, *Hibiscus rosa-sinensis*, *Tamarindus indica*, *Moringa oleifera* and *Murraya koenigii* leaves [88], and *Ailanthus altissima* leaf [89], which have demonstrated a dosage-dependent antioxidant activity in all ZnO-NPs produced by the green process.

The IC50 value measures the concentration of antioxidants needed to capture and decrease 50% of the DPPH free radical. This value is derived by analyzing the plot of percentage inhibition against concentration using linear regression (see Figure 10b). A lower IC50 value indicates more activity. The IC50 value of any substance is often compared to those of standard antioxidants. Figure 10b displays the IC50 values of the tested products (ZnO-NPs and ascorbic acid), which are represented in 10.52mg mL^{-1} and 10.88 µg mL^{-1}. The results demonstrate that the IC50 (10.53 mg mL^{-1}) of ZnO-NPs is greater than that of ascorbic acid (10.88 µg mL^{-1}), indicating a moderate antioxidant capacity compared to the conventional antioxidant. The ZnO-NPs antioxidant activity dispersed in a non-aqueous solution is attributed to the electron transfer to DPPH radicals [89].

2.8. Antibacterial Activity of ZnO-NPs

The antimicrobial efficacy of ZnO-NPs produced by using an extract derived from the peel of Citrus limon was assessed using the well diffusion method against five reference bacterial strains: *Escherichia coli* (ATCC 8739) and *Pseudomonas aeruginosa* (ATCC 9027) as Gram-negative bacteria, and *Bacillus subtilis* (ATCC 6633), *Staphylococcus aureus* (ATCC 6538), and *Listeria monocytogenes* (CIP 82110) as Gram-positive bacteria. Zinc acetate and gentamycin solutions were used as positive controls.

All five bacterial strains tested showed sensitivity to the two molecules used as positive controls. With gentamycin (1 mg mL^{-1}), the strains tested showed sensitivity with diameters ranging from 28 to 36 mm. These strains also showed sensitivity to zinc acetate solution (5 mg mL^{-1}), with inhibition zone diameters ranging from 30 to 34 mm, except for *P. aeruginosa*, which showed low sensitivity to zinc acetate solution with a diameter of 12 mm (Figure S2, Table 3).

Table 3. Diameter of Inhibition Zones (DIZ) of different ZnO-NP concentrations against bacterial strains.

| Bacterial Strains | Diameters of Growth Inhibition Zones [mm] at Different Concentrations [mg mL^{-1}] | | | | | | | | | |
| | ZnO-NPs | | | | | | | | Gentamicin | AcZn |
	1.25	2.5	5	10	25	50	75	100	1	5
S. aureus	13	15	18	20	17	19	17	22	30	34
B. subtilis	13	13	15	16	15	20	20	20	36	32
L. monocytogenes	10 SZ *	10 SZ *	8.5	10	12	14	16.5	18.5	28	30
E. coli	<6	<6	<6	<6	9	12	11	13	28	30
P. aeruginosa	<6	<6	<6	<6	<6	<6	<6	<6	34	12

SZ *: Slow-Growth Zone.

The antibacterial power of ZnO-NPs was recorded against all Gram-positive bacterial strains, notably with *S. aureus*, where inhibition zone diameters ranged from 13 to 22 mm, and *B. subtilis*, where the range of inhibitory diameters observed was between 13 and 20 mm. On the other hand, with *L. monocytogenes*, inhibition zones were only observed with ZnO-NP concentrations exceeding 5 mg mL^{-1} with diameters ranging from 8.5 to 18.5 mm. However, for low concentrations of 1.25 and 2.5 mg mL^{-1}, *L. monocytogenes* showed low activity with bacterial growth slowing zones of 10 mm diameter.

The Gram-positive strain of *E. coli* showed sensitivity to synthesized ZnO-NPs, with inhibition diameters of 9 to 13 mm only at higher ZnO-NPs concentrations above 25 mg mL^{-1}. In contrast, the resistance to these nanoparticles was observed at low concentrations of *E. coli* and at all concentrations of the *P. aeruginosa* tested strain.

Various research teams have reported that ZnO-NPs exhibit broad antibacterial activity against both Gram-positive and Gram-negative bacteria, with antibacterial efficacy increasing in a dosage-dependent manner. In a study carried out by Ahmad et al. [90], ZnO-NPs synthesized using *Mentha piperata* aqueous extract showed dosage-dependent antibacterial effects specifically targeting two strains of Gram-negative bacteria, *Pseudomonas aeroginosa* and *Proteus mirabilis*, with maximum activity observed at the highest concentration tested, 100 μg mL^{-1}, with inhibition zone diameters of 34.16 ± 2.3 mm and 39.33 ± 3.39 mm, respectively. The ZnO-NPs synthesized using the ethanolic extract of a mixture of the three parts of the *Cordia myxa* plant—leaves, roots and fruits—exhibited antibacterial effects on both Gram-positive and Gram-negative bacteria [91]. However, another study carried out on the antibacterial activity of ZnO-NPs synthesized using aqueous extracts from two parts of the *Berberis tinctoria* plant, the leaves and fruits separately, found that NPs produced using aqueous extracts from the fruits showed significant antibacterial efficacy against both Gram-positive and Gram-negative bacteria, with inhibition zone diameters ranging from 12 to 18 mm for Gram-negative bacteria, and from 12 to 19 mm for Gram-positive bacteria. NPs synthesized using aqueous fruit extracts exhibited strong antibacterial effects against Gram-positive bacteria compared to Gram-negative bacteria, with inhibition zone diameters ranging from 8 to 18 mm for Gram-negative bacteria and 13 to 19 mm for Gram-positive bacteria using NPs with concentrations ranging from 50 to 150 μg mL^{-1} [92]. This suggests that the part of the plant used to prepare the extract serving as a reducing agent for NPs could influence the potency of the antibacterial effect, as well as their spectrum. Abu ElGasim et al. [93] demonstrated that ZnO-NPs synthesized using ethanolic extract of *Lavandula pubescens* exhibited superior activity against Gram-positive bacteria *S. aureus* over Gram-negative bacteria *P. aerugenosa*, with inhibition zone diameters of 10.50 and 6.13 mm, respectively. The study carried out by Mahmure et al. [94] on ZnO-NPs synthesized using an aqueous extract of *Celosia Cristata* also showed that ZnO-NPs exhibited greater antibacterial effectiveness against Gram-positive bacteria than Gram-negative bacteria. This activity increased with both the calcination temperature, rising from 100 to 500 °C, and the volume of extract used in NP synthesis. Similarly, the study carried out by Umavathi et al. [95] reported significant antibacterial activity of ZnO-NPs synthesized using an ethanolic extract of *Justicia procumbense*, particularly against *E. coli* and *S. aureus*, while showing very low activity against *P. aerugenosa*. This low activity against *P. aerugenosa* was also observed with ZnO-NPs synthesized using the ethanolic extract of *Lavandula pubescens* [93]. These findings suggest that *P. aerugenosa* strains may exhibit only moderate sensitivity to ZnO-NPs.

In contrast to the other strains tested in our investigation, the *P. aeruginosa* strain (ATCC 9027) was less susceptible to the precursor used in the NPs synthesis (zinc acetate). This may clarify why this stain of *P. aeruginosa* was resistant to the ZnO-NPs synthesized using *Citron lemon* extract. The difference in the strength of the antibacterial effect of NPs between Gram-negative and Gram-positive bacteria can be related to variations in their surface electrostatic force, composition, and cell wall structure. ZnO nanomaterials have been receiving much attention recently because of their impressive antibacterial effects. The antibacterial activity of ZnO nanomaterials arises from their unique physicochemical characteristics, such as high surface area, large surface-to-volume ratio, and the release

of zinc ions (Zn^{2+}) in aqueous environments at low pH medium [96]. The antimicrobial activity of NPs can be affected by several factors, namely the susceptibility and type of microorganisms (Gram-negative and Gram-positive bacteria), particle size, morphology, the coating agent used for nanoparticle synthesis, and the concentration of ZnO-NPs [97].

Concerning the antibacterial mechanism of ZnO-NPs, our proposal (Figure 11) involves the production of reactive oxygen species (ROS), including hydroxyl radicals ($^\bullet$OH) and superoxide radicals (O$_2$$^{\bullet-}$), through the use of zinc oxide nanoparticles (ZnO-NPs), when these latter are exposed to environmental factors [98]. It has been reported that in the presence of a radical scavenger, the bactericidal effect of ZnO-NPs can be suppressed, providing direct evidence of the antibacterial effect mediated by ROS [96]. The release of zinc ions (Zn^{2+}) into their environment following ultraviolet (UV) or visible-light activation is likely involved in the generation of reactive oxygen species and, therefore, indirectly involved in the antibacterial mechanism induced by ZnO-NPs [99]. These ROS are known as extremely reactive molecules that have the potential to harm various cellular components, such as proteins, lipids, and DNA. We propose that the production of extracellular oxidative stress plays a role in the antibacterial effects of ZnO-NPs.
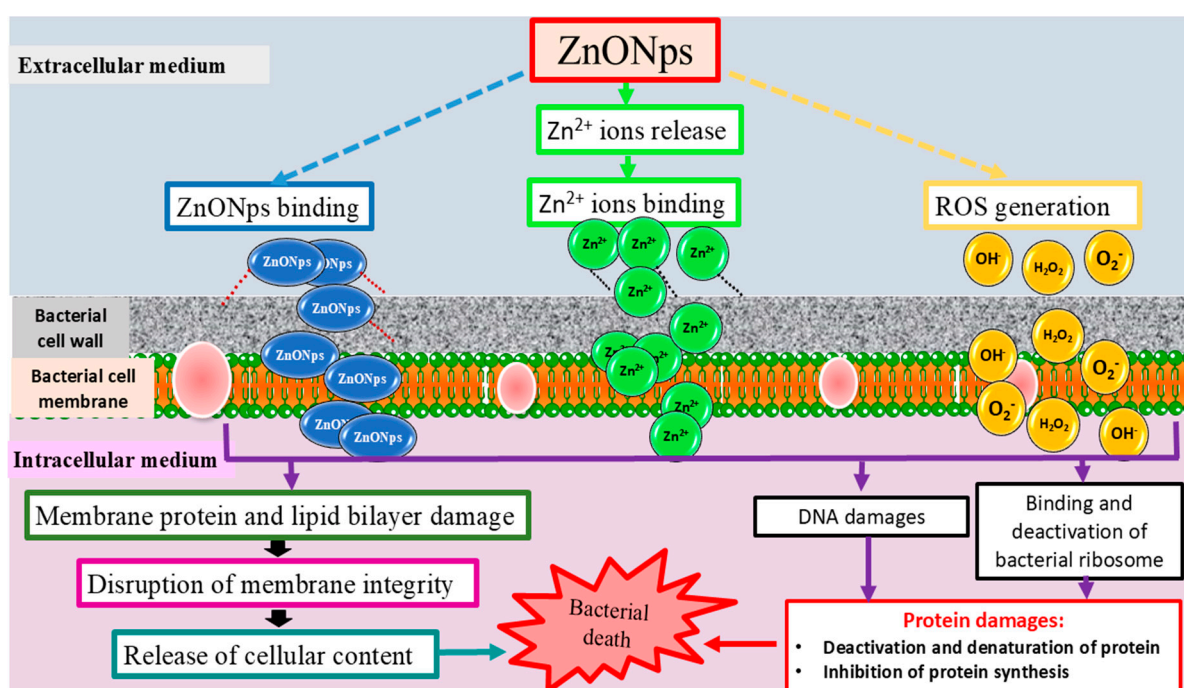

Figure 11. Schematic representation of bacterial death mechanism caused by ZnO-NPs disrupting bacterial cell membrane integrity and protein damages.

In addition, we suggest that ZnO-NPs can exert antibacterial effects through direct interaction with bacterial cells. The large surface area of ZnO-NPs allows direct physical contact with bacterial cells, leading to cell membrane rupture, leakage of intracellular components, cell lysis, and, ultimately, bacterial cell death [100]. It has been reported that ZnO-NPs increase the membrane permeability of bacterial cells [101], and that ZnO-NPs are internalized in a dose-dependent manner by mechanisms such as specific diffusion (via porins) through the silCBA gene transport system, non-specific membrane damage, and non-specific diffusion [102,103]. Research has demonstrated that ZnO-NPs are significantly internalized and distributed almost uniformly within bacterial cells, causing damage at the membrane level and changes in the morphology of bacterial cells [104,105]. Once internalized, zinc oxide nanoparticles or Zn^{2+} ions can trigger the process of cellular apoptosis. Cell death could be triggered either by the direct contact of Zn^{2+} ions or ZnO-NPs with the different extra/intracellular components or following the generation of

oxidative stress inside the bacterial cells. In the intracellular compartment, ROS and Zn^{2+} ions can lead to DNA, protein, and lipid bacterial damage, impairing their vital functions and thereby contributing to bacterial death [103,106]. They can mediate disruption of the bacterial cell membrane by modifying either proteins involved in membrane structure or the activity of enzymatic proteins. They also inhibit DNA/plasmid and protein/enzyme replication in cells [23,107].

2.9. Gaussian Process Regression

In this study, fine-tuning the kernel model has been pivotal in identifying the most efficient model for predicting the photodegradation rate of QY by ZnO-NPs. A thorough examination of 10 different kernel functions was conducted, and their parameters, including the kernel scale denoted by [SigmaM, SigmaF], as well as sigma, were carefully optimized using the FDB-LFD algorithm. This meticulous process enabled us to assess each model's ability to capture the complex relationships within our dataset. Consequently, the most suitable model was selected, ensuring the reliability and accuracy of our predictions for the QY photodegradation rate based on the R and RMSE values obtained during each phase. Following the optimization of the kernel function, the details of the most effective model are provided in Table 4.

Table 4. Performance of the best GPR_FDB-LFD model.

Kernel Function	Basis Function	Kernel Scale		*Sigma*	R				RMSE			
		SigmaM	SigmaF		Train	Test	Val	ALL	Train	Test	Val	ALL
ARD-Exponential	Constant	1.0374	4.1118	0.2500	0.9999	0.9999	0.9999	0.9999	0.0160	0.0250	0.0244	0.0179
		7.8652										
		6.9035										
		5.2877										

The results of optimizing the GPR model using the FDB-LFD algorithm demonstrate exceptional predictive performance. The model utilizing the ARD-Exponential kernel function with a constant basis function yielded extremely high correlation coefficients for all phases of the model: training, testing, validation, and the entire dataset. A correlation coefficient close to 1 (0.9999 in each phase) indicates a strong correlation between the predicted values by the model and the actual values observed in the data, underscoring the model's ability to effectively capture relationships between input and output variables.

Moreover, the RMSE values are very low for all phases of the model, confirming the high accuracy of predictions. For the training phase, the RMSE is 0.0160, for the testing phase it is 0.0250, and for the validation phase it is 0.0244. Finally, for the entire dataset, the RMSE is 0.0179. These RMSE values, all closer to zero, indicate that the model's predictions are very close to the actual values, thereby enhancing its reliability and accuracy.
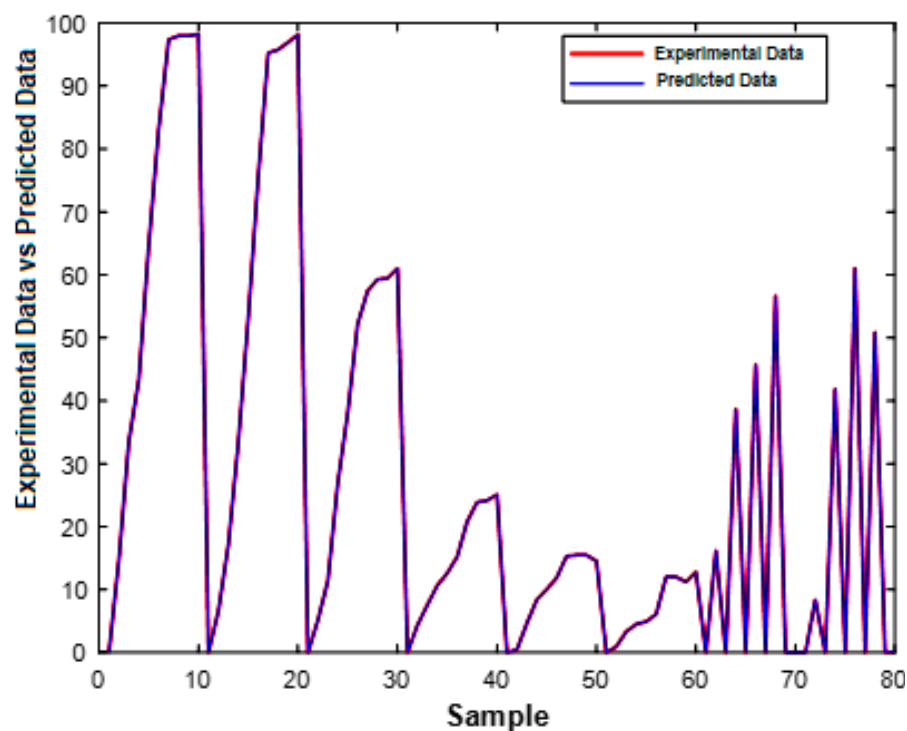
These results underscore the high performance and precision of the GPR model optimized with the FDB-LFD algorithm, employing the ARD-Exponential kernel function with a constant basis function, in predicting the photodegradation rate of QY by ZnO-NPs.

These outcomes are visually represented in Figure S3, portraying the performance metrics of the optimized GPR_FDB-LFD model.
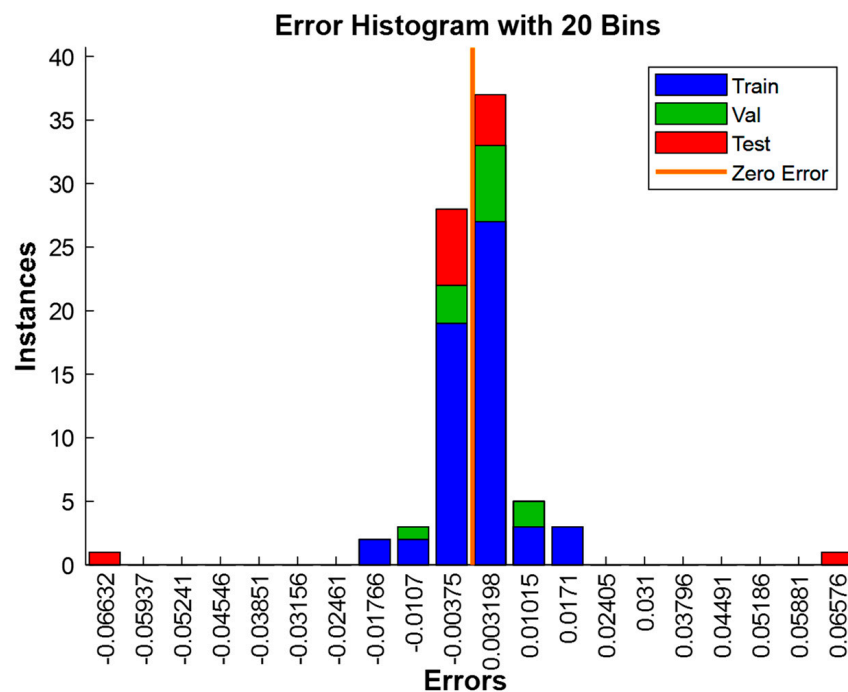
2.9.1. Residue Analysis

To delve deeper into the GPR_FDB-LFD model and further validate its effectiveness, the residual analysis method was employed [108,109]. This involved two distinct approaches. First, the degradation rates of QY were juxtaposed with the corresponding ed values and plotted on a graph (Figure 12a). Second, a histogram of model residues was produced, illustrating the distribution of errors for each phase beneath histograms

(Figure 12b). These analyses were instrumental in evaluating the accuracy and reliability of the model by visually comparing predicted values with actual degradation rates and analyzing the distribution of errors across the model's various phases.

(**a**)

(**b**)

Figure 12. Residuals relating to the models established by the different techniques according to the estimated values: (**a**) relationship between experimental data and the predicted data of samples, and (**b**) histogram of model errors.

The results presented in Figure 12a show a strong alignment between the experimental and predicted values, underscoring the high accuracy of the GPR_FDB-LFD model in forecasting QY degradation rates. This close match between predictions and experimental data validates the model's ability to accurately capture trends and variations within the dataset.

Furthermore, Figure 12b highlights that all prediction errors follow normal distribution with zero mean and are clustered within a very close range to zero on the horizontal axis. This observation suggests that the model's predictions are generally highly accurate, with minimal errors. These findings thus confirm the remarkable effectiveness of the GPR_FDB-LFD model in predicting QY degradation rates. In summary, the tight overlap between experimental and predicted values in Figure 12a, coupled with the narrow normal distribution of errors around zero in Figure 12b, underscores the robustness and reliability of the GPR_FDB-LFD model in accurately predicting QY degradation rates.

2.9.2. Optimization of the Operating Condition and Validation

To pinpoint the optimal conditions at an initial concentration of $15\,\mathrm{g\,L^{-1}}$, we employed the improved Lévy flight distribution algorithm (FDB-LFD). This advanced algorithm [38] represents a refined version of the Lévy flight distribution algorithm, integrating an FDB (Firefly-Dragonfly-Based) guiding mechanism. Once the optimal conditions were determined, experimental validation was pursued in the laboratory to ascertain the model's effectiveness. To achieve this, we calculated the error between the experimental QY degradation rate and the predicted rate. Table 5 provides the details on the optimal conditions, along with the predicted and experimental values, as well as the error between them.

Table 5. Results of optimization and validation.

Agent Search Number: 50 Number of Iterations: 100	
Concentration of QY: 15 mg L^{-1}	
Optimal condition	X1 = 300 min, X2 = 15 mg L^{-1}, X3 = 0.3 g, and X4 = 9
Predicted QY photodegradation rate	98.1428%
Experimental QY photodegradation rate	98.1316%
Error	0.0112%

The results from the application of the FDB-LFD algorithm reveal several key insights. First, the algorithm conducted 100 iterations with an agent search number of 50 to identify the optimal conditions for QY photodegradation. The optimization results showed that the most effective parameters for achieving maximum degradation efficiency were a contact time of 300 min, an initial QY concentration of $15\,\mathrm{mg\,L^{-1}}$, a catalyst dose of $0.3\,\mathrm{mg\,L^{-1}}$, and a pH of 9.

Upon application of these optimal conditions, the model predicted a QY photodegradation rate of 98.1316%. Subsequently, experimental validation conducted in the laboratory closely mirrored this prediction, resulting in an observed QY photodegradation rate of 98.1428%. The minimal error between the predicted and experimental values, amounting to only 0.0112%, underscores the high accuracy and reliability of the model in forecasting QY photodegradation rates under the specified conditions.

In essence, these results demonstrate the effectiveness of the FDB-LFD algorithm in determining optimal conditions for QY photodegradation, with the model's predictions closely aligning with experimental outcomes. This suggests that the optimization based on the GPR model offers a robust framework for achieving efficient QY degradation, thereby highlighting the utility of the model in environmental remediation applications.

2.9.3. Interface for Optimization and Prediction

In this study, a user-friendly MATLAB-based application has been meticulously crafted to revolutionize the optimization process for determining optimal conditions associated

with the concentration of QY and forecasting the QY degradation rate catalyzed by ZnO-SPs, leveraging the sophisticated GPR_FDB-LFD model and FDB-LFD algorithm (see Figure 13). This innovative application simplifies and expedites the optimization task. Users are empowered to input specific parameters (inputs), thereby unlocking a realm of precise predictions regarding degradation rates. By seamlessly integrating the GPR_FDB-LFD model into this cutting-edge application, researchers and environmental practitioners alike can embark on a journey toward pinpointing optimal conditions for QY degradation with unparalleled efficiency and efficacy, thus ushering in a new era of environmental remediation prowess.
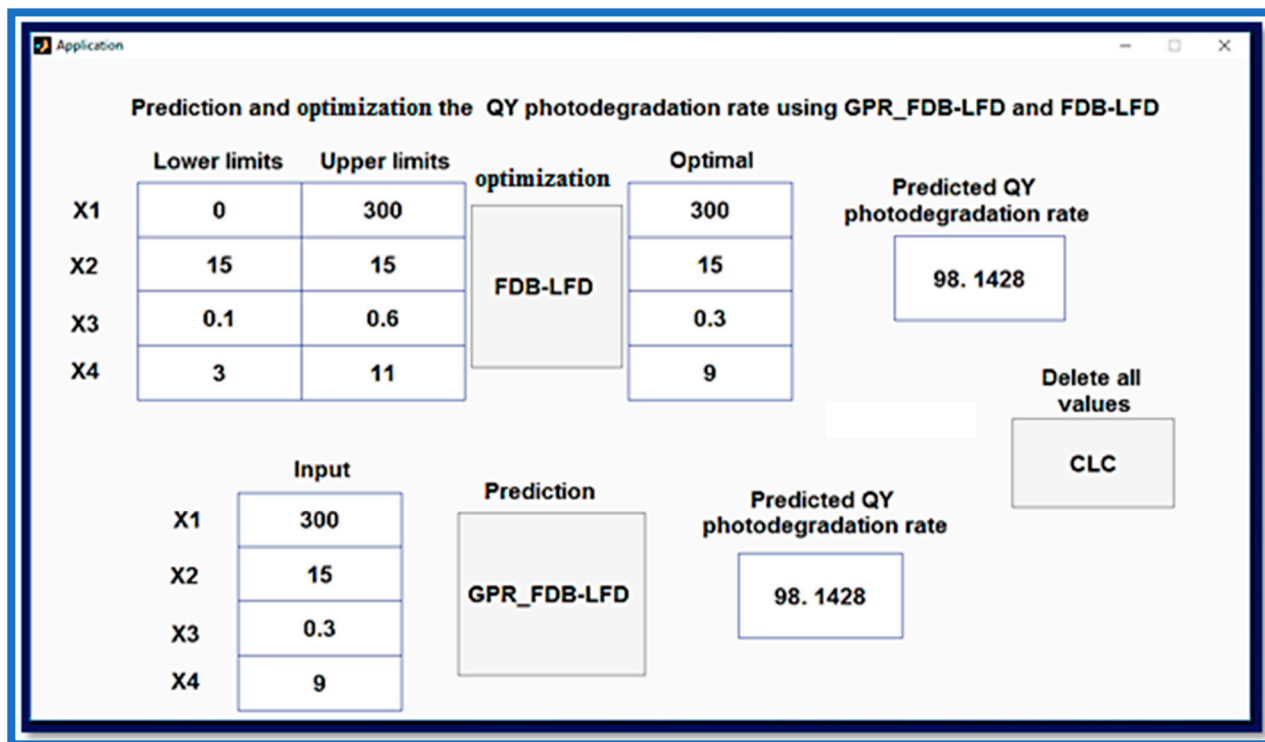

Figure 13. Application for prediction and optimization of QY photodegradation rate using the GPR_FDB-LFD and FDB-LFD.

3. Materials and Methods

3.1. Materials

The materials used included zinc acetate dehydrates ($Zn(CH_3COO)_2$ $2H_2O$, 99%, Merck, (Darmstadt, Germany), citric acid ($C_6H_8O_7$, 99.5%, Merck, Darmstadt, Germany), ethanol (C_2H_6O, 98%, Biochem Chemopharma, Cosne-sur-Loire, France), ammonium hydroxide (NH_4OH, 30%, Merck (Darmstadt, Germany)), ethylene glycol ($C_2H_4(OH)_2$, 97.5%, Sigma Aldrich, Saint. Louis, MO, USA), quinolone yellow (E104) (QY) provided by the Hinckel industry in Chéraga, Algeria, Muller Hinton broth (Liofilchem, Via Scozia, Roseto degli Abruzzi TE, Italy), and 2,2-diphenyl-1-picryl-hydrazyl DPPH ($C_{18}H_{12}N_5O_6$, 90%, Sigma-Aldrich). All chemical reagents used in the experiments or in the synthesis were of analytical grade and were used as received.

The five bacterial strains used to assess the antimicrobial activity of ZnO-NPs were provided by the SAIDAL pharmaceutical industry of Algeria. These strains included *Pseudomonas aeruginosa* (ATCC 9027), *Escherichia coli* (ATCC 8739), *Staphylococcus aureus* (ATCC 6538), *Bacillus subtilis* (ATCC 6633), and *Listeria monocytogenes* (CIP 82110).

3.2. Methods

3.2.1. Preparation of Peel Extracts

For the extract preparation, the peels of *Citrus limon* (C. LP) were carefully washed multiple times with distilled water to ensure the removal of any dirt. An appropriate quantity of fresh *C. lemon* peel of 100 g was then chopped into small pieces and tempered in sufficient distilled water in a flask. After 2 h of extracting essential oils (EO) using Clevenger-type hydro-distillation, the EO extract was separated from the hydrosol through decantation and filtration, using Whatman filter paper number 1. The aqueous solution of *C. limon peel* from the pure extract was then stored in a bottle at 4 °C for further use.

3.2.2. ZnO-NPs Green Synthesis

A sol-gel-mediated green synthesis process was used to synthesize the ZnO-NPs. A 0.1 M concentration of $Zn(CH_3COO)_2$-$2H_2O$ was initially dissolved in 40 mL of distilled water in a dry glass beaker after 1 h of continuous magnetic stirring at room temperature. Subsequently, 10 mL of ethylene glycol (EG) was added, keeping the solution temperature constant at 60 °C. Then, 5 mL of aqueous NH_4OH was added to the reactant mixture and stirred for 2 h at room temperature.

Following this, a 10% *C. lemon* peel extract (volumetric ratio) was dropped to the previous mixture solution and aged at 60 °C for 24 h until yellowish aerogel was observed. After increasing the heating temperature to 110 °C, a cake was formed. After subsequent drying, the final yield was ready for further studies. Finally, the collected powders were oven-dried at 120 °C for 24 h, then ground and annealed at 500 °C for 2 h in a muffle furnace with air atmosphere to transform to ZnO-NPs. The obtained powder was homogenized, using agate mortar, into fine NP powder and sieved for further characterization and applications.

3.2.3. Characterization of ZnO-NPs

Thermal gravimetric analysis (TGA) and differential thermal analysis (DTA) were performed on the catalyst in its initial state prior to calcination, using the TEA SDTQ 600 instrument (TA Instruments, New Castle, DE, USA). The sample was subjected to heating at a rate of 10 °C per minute until reaching a final temperature of 1100 °C in the presence of N_2 gas. During this process, the weight loss resulting from the increase in temperature was measured. Additionally, the prepared ZnO-NP powders were characterized by X-ray diffraction with a Bruker (Bremen, Germany) D8 X-ray diffractometer (XRD), using Cu Kα radiation (λ = 1.54178 A). The analysis was carried out in the range of 5 to 85°, and phase identification was performed using HighScore Plus software, version 3.0d. The morphology and chemical composition of the ZnO-NPs were studied using a Jeol (Tokyo, Japan) JSM-7200F scanning electron microscope (SEM/EDS). Fourier transform infrared (ATR-FTIR) spectroscopy was employed to identify the functional groups on the NP catalyst using ATR-FTIR with Brucke Alpha One spectroscopy (Bruker, Bremen, Germany). The determination of optical properties was used to evaluate the bandgap energy. This was performed by a UV-visible spectrophotometer (Specord 210 Analytical Jena, Jena, Germany), and the measure was recorded between 190 to 1100 nm. The specific surface area of ZnO-NPs was analyzed using the Brunauer–Emmett–Teller (BET) method, using the ASAP 2020 Micromeritics apparatus (Micromeritics, Norcross, GA, USA) after degassing at 300 °C for 4 h. The particle size of ZnO-NPs was obtained using diffraction laser size analysis (DLS) (HORIBA SZ-100, Irvine, CA, USA). To further investigate the screening of ZnO-NPs properties, Raman spectroscopy was performed using a HORIBA LABRAM HR Raman spectrometer in single spectrograph mode using a holographic dispersive grating of 600 grooves mm^{-1}, providing a complementary technique to identify the obtained chemical phase. In addition, the Hanna 2211 pH meter (Bangkok, Thailand) was used to accurately measure the pH of the liquid medium, and the Shimadzu 1800 UV-vis spectrophotometer (Kyoto, Japon) was used for monitoring the dye concentration.

3.2.4. Photodegradation Experiments

The photocatalytic degradation of the quinolone yellow (QY) dye by ZnO-NPs was observed under direct sunlight irradiation as a simple photochemical reactor. Thus, a known mass of synthesized catalytic nano-powders was dispersed and homogenized in an aqueous dye QY at a known initial concentration. The solution's pH was defined, and the mixture was homogenized in the dark for 1 h in order to reach adsorption–desorption equilibrium. The solution temperature was maintained at a constant value of 25 °C using a circular bath. The ZnO nano-powder dye mixture was then exposed to direct sunlight. At regular time intervals, samples were taken to assess the remaining dye concentration in the solution. Before analysis, the catalyst powder was separated by centrifugation, and the absorbance at a λ_{max} wavelength of 414 nm was measured; subsequently, the residual concentration was calculated to estimate the dye photodegradation rate and efficiency (R%) using the following equation [110]:

$$R\% = \left(\frac{C_o - C_t}{C_o}\right) \times 100 \tag{7}$$

where C_o and C_t (mg L^{-1}) are concentrations at the initial time and at time (t), respectively.

3.2.5. Antibacterial Activity of Biosynthesized ZnO-NPs

The antibacterial potential of biosynthesized ZnO-NPs was assessed against five bacterial strains: *Pseudomonas aeruginosa* (ATCC 9027), *Escherichia coli* (ATCC 8739), *Staphylococcus aureus* (ATCC 6538), *Bacillus subtilis* (ATCC 6633), and *Listeria monocytogenes* (CIP 82110). To carry out this, young bacterial cultures (24 h) were added to Muller Hinton broth to prepare a bacterial suspension. The suspension's turbidity was then adjusted to an OD 625 nm of 0.08–0.13, which gives approximately 10^8 CFU ml^{-1} [111].

The bacterial suspension was then inoculated using a swab on the surface of the Petri dishes previously poured with a semi-solid Muller Hinton agar medium. After creating wells in this agar using a sterile Pasteur pipette, they were filled with different concentrations of ZnNPs (100, 75, 50, 25, 10, 5, 2.5, and 1.25 mg mL^{-1}). This test used zinc acetate and gentamycin solutions as positive controls. To improve the dispersion of ZnO-NPs in agar, the Petri dishes were first incubated at 4 °C for a duration of 2 h, followed by incubation at 37 °C for 24 h. The antibacterial effect of ZnO-NPs was evaluated by measurement of the Diameter of Inhibition Zones (DIZ) around the wells using a grouting foot (the diameter of the wells is included).

3.2.6. Antioxidant Activity

The free radical-scavenging activity of synthesized ZnO was evaluated using the DPPH antioxidant assay [112]. Briefly, 200 µL of the prepared ZnO solution with different concentrations ranging from 0 to 20 mg L^{-1} was added to 800 µL of 0.1 mM DPPH solution and left to incubate for 30 min at room temperature. Using a Specord 210 UV-visible spectrophotometer, the absorbance was taken at a wavelength of 517 nm, in the absence (A_0) and presence of the standard (ascorbic acid) or ZnO-NPs (A_1). The antioxidant activity was evaluated by calculating the % of DPPH scavenging (inhibition %) as follows [113]:

$$\% \text{ Scavenging[DPPH]} = \frac{[A_0 - A_1]}{A_0} \times 100 \% \tag{8}$$

The IC50 was determined by analyzing the inhibition rate (I %) at various concentrations of ZnO-NPs using GraphPad Prism 9 software.

3.2.7. Gaussian Process Regression

Gaussian Process Regression (GPR) is a sophisticated machine learning method designed for modeling and predicting continuous data [114]. Unlike more conventional techniques such as linear regression, GPR does not rely on an assumption of linearity

between input and output variables. Instead, it leverages the joint probability distribution of the training data to estimate the probability distribution of predictions [115]. One of the major advantages of GPR lies in its ability to provide probabilistic predictions. Unlike other regression methods that yield a single prediction value for each input, GPR provides a probability distribution for each prediction. This feature not only offers an estimation of the predicted value but also a measure of the uncertainty associated with that prediction [116]. This capability is particularly valuable in domains where an accurate assessment of uncertainty is crucial, such as finance, healthcare, and environmental sciences [117]. Moreover, GPR stands out for its high flexibility and adaptability to various regression problems [118]. It can handle datasets of variable sizes as well as nonlinear relationships and complex dependencies between variables. Additionally, it is robust against noisy data and can provide accurate estimates even in the presence of outliers [119]. Furthermore, a major strength of GPR is its non-requirement of an explicit specification of a model function. This characteristic makes it particularly effective in cases where the relationship between input and output variables is not fully understood [115]. By adjusting the covariance of the training data, GPR can capture complex patterns in the data and provide accurate predictions even without a complete understanding of the underlying system [114].

In this study, GPR was utilized to develop a mathematical model for the degradation of the dye QY by ZnO-NPs. These NPs were synthesized using green chemistry, employing an aqueous extract of lemon zest as a mediator reagent in the sol-gel method. The optimization parameters for photodegradation efficiency were set as the model inputs: X1: Contact time (0–300 min), X2: Initial QY concentration (10–50 mg L^{-1}), X3: Catalyst dose (0.1 to 0.6 mg L^{-1}), X4: Solution pH (3–11). Meanwhile, the QY photodegradation rate was used as the model output (Y1). Once the database was created, it was normalized to the range [−1,1]. Subsequently, the database was divided into three subsets: 70% for training, 15% for testing, and 15% for validation. To identify the most suitable model, an extensive exploration of 10 kernel functions was conducted, including exponential, squared exponential, Matern32, Matern52, rational quadratic, ARD exponential, ARD squared exponential, ARD Matern32, ARD Matern52, and ARD rational quadratic kernels. Moreover, significant attention was devoted to fine-tuning the parameters of each kernel function, including the kernel scale denoted by [sigmaM, sigmaF] and sigma itself. To accomplish this task, the improved Lévy flight distribution algorithm (FDB-LFD) was utilized to optimize the specific parameters of each kernel function. FDB-LFD, introduced by Bakir et al. in 2022 [38], represents an enhanced version of the Lévy flight distribution algorithm incorporating an FDB (Firefly-Dragonfly-Based) guiding mechanism.

The following ten kernel functions were used in this work [114,115]:

- Squared Exponential Kernel

$$k\left(x_i, x_j | \theta\right) = \sigma_f^2 exp\left[-\frac{1}{2}\frac{\left(x_i - x_j\right)^T\left(x_i - x_j\right)}{\sigma_l^2}\right] \tag{9}$$

where: σ_l is the characteristic length scale and σ_t is the signal standard deviation.

- Exponential Kernel

$$k\left(x_i, x_j | \theta\right) = \sigma_f^2 exp\left[-\frac{r}{\sigma_l}\right] \tag{10}$$

where σ_l is the characteristic length scale and $r = \sqrt{\left(x_i - x_j\right)^T\left(x_i - x_j\right)}$.

- Matern 3/2

$$k\left(x_i, x_j | \theta\right) = \sigma_f^2\left(1 + \frac{\sqrt{3}r}{\sigma_l}\right)exp\left(-\frac{\sqrt{3}r}{\sigma_l}\right) \tag{11}$$

where

$$r = \sqrt{\left(x_i - x_j\right)^T \left(x_i - x_j\right)} \tag{12}$$

- Matern 5/2

$$k\left(x_i, x_j | \theta\right) = \sigma_f^2 \left(1 + \frac{\sqrt{5}r}{\sigma_l} + \frac{5r^2}{3\sigma_f^2}\right) exp\left(-\frac{\sqrt{5}r}{\sigma_l}\right)$$

where:

$$r = \sqrt{\left(x_i - x_j\right)^T \left(x_i - x_j\right)} \tag{13}$$

- Rational Quadratic Kernel

$$k\left(x_i, x_j | \theta\right) = \sigma_f^2 \left(1 + \frac{r^2}{2\alpha\sigma_l^2}\right)^{-\alpha} \tag{14}$$

where: σ_l is the characteristic length scale, α is a positive-valued scale mixture parameter. $r = \sqrt{\left(x_i - x_j\right)^T \left(x_i - x_j\right)}$.

- ARD Squared Exponential Kernel

$$k\left(x_i, x_j | \theta\right) = \sigma_f^2 exp\left[-\frac{1}{2}\sum_{m=1}^{d} \frac{\left(x_{im} - x_{jm}\right)^2}{\sigma_m^2}\right] \tag{15}$$

- ARD Exponential Kernel

$$k\left(x_i, x_j | \theta\right) = \sigma_f^2 exp(-r)$$

where

$$r = \sqrt{\sum_{m=1}^{d} \frac{\left(x_{im} - x_{jm}\right)^2}{\sigma_m^2}} \tag{16}$$

- ARD Matern 3/2

$$k\left(x_i, x_j | \theta\right) = \sigma_f^2 \left(1 + \sqrt{3}r\right) exp\left(-\sqrt{3}r\right)$$

where

$$r = \sqrt{\sum_{m=1}^{d} \frac{\left(x_{im} - x_{jm}\right)^2}{\sigma_m^2}} \tag{17}$$

- ARD Matern 5/2

$$k\left(x_i, x_j | \theta\right) = \sigma_f^2 \left(1 + \sqrt{5}r + \frac{5}{3}r^2\right) exp\left(-\sqrt{5}r\right)$$

where

$$r = \sqrt{\sum_{m=1}^{d} \frac{\left(x_{im} - x_{jm}\right)^2}{\sigma_m^2}} \tag{18}$$

- ARD Rational Quadratic Kernel

$$k\left(x_i, x_j | \theta\right) = \sigma_f^2 \left(1 + \frac{1}{2\alpha}\sum_{m=1}^{d} \frac{\left(x_{im} - x_{jm}\right)^2}{\sigma_m^2}\right)^{-\alpha} \tag{19}$$

Moreover, significant attention was devoted to fine-tuning the parameters of each kernel function, including the kernel scale denoted by [sigmaM, sigmaF] and sigma itself. To accomplish this task, the improved Lévy flight distribution algorithm (FDB-LFD) was utilized to optimize the specific parameters of each kernel function (Figure 14). FDB-LFD, introduced by Bakir et al. in 2022 [38], represents an enhanced version of the Lévy flight distribution algorithm incorporating an FDB (Firefly-Dragonfly-Based) guiding mechanism [38].
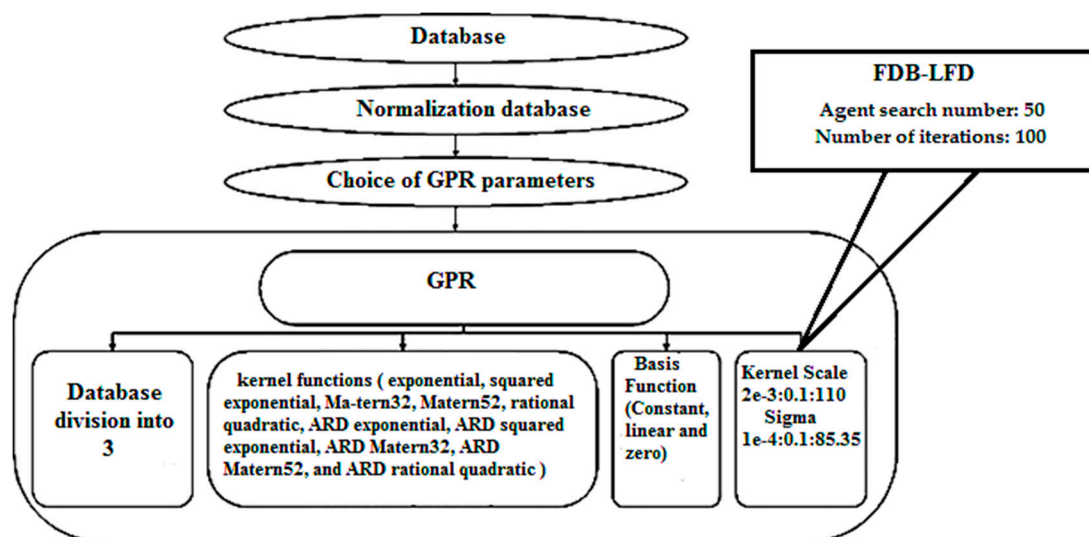

Figure 14. Organization chart for the development and optimization of the GPR_FDB-LFD.

The effectiveness of each model was rigorously assessed using key performance measures, particularly the correlation coefficient (R) and root mean square error (RMSE), calculated using the following formulas [120–125]:

$$R = \frac{\sum\limits_{i=1}^{N} \left(y_{\exp} - \overline{y}_{\exp}\right)\left(y_{pred} - \overline{y}_{pred}\right)}{\sqrt{\sum\limits_{i=1}^{N}\left(y_{\exp} - \overline{y}_{\exp}\right)^2 \sum\limits_{i=1}^{N}\left(y_{pred} - \overline{y}_{pred}\right)^2}} \tag{20}$$

$$RMSE = \sqrt{\left(\frac{1}{N}\right)\left(\sum\limits_{i=1}^{N\sum}\left[\left(ypred_{exp}()\right)[]^2\right]()\right)} \tag{21}$$

where N is the number of data samples, y_{exp} and y_{pred} are the experimental and predicted values, respectively, and $\bar{y}_{exp}$ and $\bar{y}_{pred}$ are the average values of the experimental and predicted values, respectively [108].

4. Conclusions

This work presents the synthesis of ZnO-NPs applying a green chemistry approach, utilizing lemon peel extract as a stabilizing and reducing agent for the sol-gel method. The produced NPs were cost-effective and ecologically sustainable. The obtained ZnO-NP powder was subjected to numerous characterization techniques, including XRD, SEM, EDS, ATR-FTIR, Raman spectroscopy, and UV-visible analysis, to assess their structural, morphological, and chemical composition, as well as their optical properties. The synthesized ZnO-NPs were also tested to evaluate their photocatalytic activity in degrading an aqueous solution of QY food dye. They were also thoroughly investigated for their antibacterial activity. Characterization data verified the formation of a pure phase of ZnO-NPs, as confirmed by XRD patterns. Using scanning electron microscopy, the nanocomposite

showed grains with irregular shapes. The bandgap energy of 3.2 eV was measured by DRS, while Raman and ATR-FTIR spectroscopy analyses offer further information regarding the composition and structure of the substance. Together, these methods serve to improve the comprehension of the characteristics of the prepared ZnO-NP material. The study demonstrates that the ZnO-NPs synthesized by green chemistry are an effective material against organic pollutants, particularly the dyes used in the investigation. Notably, photodegradation of the QY dye under sunlight was influenced by operating parameters such as pH, the amount of catalyst concentration, and initial QY dye concentration. Higher initial dye concentrations reduced the photodegradation yield and the rate constant of the reaction, while basic pH levels improved degradation rates. Additionally, the kinetics of photodegradation of QY under direct sunlight followed a first-order model, with kinetic constants for adsorption equilibrium and photodegradation being Kc (6.632×10^{-2} L mg^{-1}) and kH (7.104×10^{-2} mg L^{-1} min^{-1}), respectively. The antimicrobial effect of ZnO-NPs exhibited the highest potency against Gram-positive bacterial strains such as *S. aureus*, *B. subtilis*, and *Listeria monocytogenes*, and the least potency against *E. coli*. The antibacterial impact was dosage- and strain-dependent for ZnO-NPs, indicating that the bacterial cell wall composition influences the nanoparticles' mode of action. The ZnO-NPs exhibited a moderate level of antioxidant activity, which increased with higher ZnO-NPs concentration and showed higher antioxidant effectiveness than standard ascorbic acid. The study underscores the advantage of using clean, renewable energy, as the photodegradation rates are considerable under sunlight, highlighting the sustainability of the process whose energy source is clean, inexhaustible, and free. Its potentialities are considerable and very diversified. The ZnO-NPs were successfully synthesized and confirmed by the various characterization techniques. These findings offer promising insights into the potential exploration of ZnO-NPs in several medicinal uses, in photocatalytic processes employing direct sunlight, and in various industrial contexts. Moreover, the integration of GPR with the improved Lévy flight distribution (FDB-LFD) algorithm provides valuable insights into the modeling of the QY photodegradation rate. The optimized model demonstrates exceptional performance in predicting QY degradation rates, with high correlation coefficients and low root mean square error values, validating its reliability and accuracy. These results present a series of major innovations in the synthesis of NPs, further emphasizing the efficacy of the GPR_FDB-LFD model in environmental remediation applications and offering a robust framework for optimizing degradation conditions and facilitating precise degradation rate predictions.

Supplementary Materials: The following supporting information can be downloaded at: https://www.mdpi.com/article/10.3390/catal14110831/s1. Figure S1. Zeta potential of ZnO-NPs (E = −53.8 mV); Figure S2. Pictorial presentation of bacterial growth inhibition by ZnO-NPs; Figure S3. Comparison between experimental and predicted values.

Data Availability Statement: The data and materials can be made available upon request from the corresponding author.

Conflicts of Interest: The authors declare no conflicts of interest.

References

1. Tahraoui, H.; Toumi, S.; Boudoukhani, M.; Touzout, N.; Sid, A.N.E.H.; Amrane, A.; Belhadj, A.-E.; Hadjadj, M.; Laichi, Y.; Aboumustapha, M. Evaluating the Effectiveness of Coagulation–Flocculation Treatment Using Aluminum Sulfate on a Polluted Surface Water Source: A Year-Long Study. *Water* **2024**, *16*, 400. [CrossRef]

2. Vinci, G.; Maddaloni, L.; Mancini, L.; Prencipe, S.A.; Ruggeri, M.; Tiradritti, M. The Health of the Water Planet: Challenges and Opportunities in the Mediterranean Area. An Overview. *Earth* **2021**, *2*, 894–919. [CrossRef]

3. Ingrao, C.; Strippoli, R.; Lagioia, G.; Huisingh, D. Water Scarcity in Agriculture: An Overview of Causes, Impacts and Approaches for Reducing the Risks. *Heliyon* **2023**, *9*, e18507. [CrossRef]

4. Kristanti, R.A.; Hadibarata, T. Phytoremediation of Contaminated Water Using Aquatic Plants, Its Mechanism and Enhancement. *Curr. Opin. Environ. Sci. Health* **2023**, *32*, 100451. [CrossRef]

5. Bhat, S.A.; Bashir, O.; UI Haq, S.A.; Amin, T.; Rafiq, A.; Ali, M.; Américo-Pinheiro, J.H.P.; Sher, F. Phytoremediation of Heavy Metals in Soil and Water: An Eco-Friendly, Sustainable and Multidisciplinary Approach. *Chemosphere* **2022**, *303*, 134788. [CrossRef]

6. Khan, M.S.; Rehman, M.T.; Bhat, S.A.; Tabrez, S.; Hussain, A.; Husain, F.M.; AlAjmi, M.F.; Alamery, S.F.; Sumbul, S. Food Additive Dye (Quinoline Yellow) Promotes Unfolding and Aggregation of Myoglobin: A Spectroscopic and Molecular Docking Analysis. *Spectrochim. Acta. A Mol. Biomol. Spectrosc.* **2019**, *214*, 216–226. [CrossRef] [PubMed]

7. Liu, X.; Wang, J. Decolorization and Degradation of Various Dyes and Dye-Containing Wastewater Treatment by Electron Beam Radiation Technology: An Overview. *Chemosphere* **2024**, *351*, 141255. [CrossRef]

8. Kumar, V.; Lakkaboyana, S.K.; Sharma, N.; Chakraborty, P.; Umesh, M.; Pasrija, R.; Thomas, J.; Kalebar, V.U.; Jayaraj, I.; Awasthi, M.K.; et al. A Critical Assessment of Technical Advances in Pharmaceutical Removal from Wastewater—A Critical Review. *Case Stud. Chem. Environ. Eng.* **2023**, *8*, 100363. [CrossRef]

9. Weiss, S.; Xu, Z.Z.; Peddada, S.; Amir, A.; Bittinger, K.; Gonzalez, A.; Lozupone, C.; Zaneveld, J.R.; Vázquez-Baeza, Y.; Birmingham, A.; et al. Normalization and Microbial Differential Abundance Strategies Depend upon Data Characteristics. *Microbiome* **2017**, *5*, 27. [CrossRef]

10. Choudoir, M.J.; DeAngelis, K.M. A Framework for Integrating Microbial Dispersal Modes into Soil Ecosystem Ecology. *iScience* **2022**, *25*, 103887. [CrossRef]

11. Gillings, M.R.; Paulsen, I.T. Microbiology of the Anthropocene. *Anthropocene* **2014**, *5*, 1–8. [CrossRef]

12. Grzegorzek, M.; Wartalska, K.; Kaźmierczak, B. Review of Water Treatment Methods with a Focus on Energy Consumption. *Int. Commun. Heat. Mass. Transf.* **2023**, *143*, 106674. [CrossRef]

13. Meese, A.F.; Kim, D.J.; Wu, X.; Le, L.; Napier, C.; Hernandez, M.T.; Laroco, N.; Linden, K.G.; Cox, J.; Kurup, P.; et al. Opportunities and Challenges for Industrial Water Treatment and Reuse. *ACS EST Eng.* **2022**, *2*, 465–488. [CrossRef]

14. Kebir, M.; Tahraoui, H.; Chabani, M.; Trari, M.; Noureddine, N.; Assadi, A.A.; Amrane, A.; Ben Hamadi, N.; Khezami, L. Water Cleaning by a Continuous Fixed-Bed Column for Cr (VI) Eco-Adsorption with Green Adsorbent-Based Biomass: An Experimental Modeling Study. *Processes* **2023**, *11*, 363. [CrossRef]

15. Madi, K.; Chebli, D.; Ait Youcef, H.; Tahraoui, H.; Bouguettoucha, A.; Kebir, M.; Zhang, J.; Amrane, A. Green Fabrication of ZnO Nanoparticles and ZnO/rGO Nanocomposites from Algerian Date Syrup Extract: Synthesis, Characterization, and Augmented Photocatalytic Efficiency in Methylene Blue Degradation. *Catalysts* **2024**, *14*, 62. [CrossRef]

16. Loeb, S.K.; Alvarez, P.J.J.; Brame, J.A.; Cates, E.L.; Choi, W.; Crittenden, J.; Dionysiou, D.D.; Li, Q.; Li-Puma, G.; Quan, X.; et al. The Technology Horizon for Photocatalytic Water Treatment: Sunrise or Sunset? *Environ. Sci. Technol.* **2019**, *53*, 2937–2947. [CrossRef]

17. Singh, K.; Maurya, S.; Gupta, S.; Ranjan, N.; Ramanathan, G.; Bhattacharya, S. Effect of the Standardized ZnO/ZnO-GO Filter Element Substrate Driven Advanced Oxidation Process on Textile Industry Effluent Stream: Detailed Analysis of Photocatalytic Degradation Kinetics. *ACS Omega* **2023**, *8*, 28615–28627. [CrossRef]

18. Mao, M.; Qi, Y.; Lu, K.; Chen, Q.; Xie, X.; Li, X.; Lin, Z.; Chai, L.; Liu, W. Selective Capacitive Recovery of Rare-Earth Ions from Wastewater over Phosphorus-Modified TiO_2 Cathodes via an Electro-Adsorption Process. *Environ. Sci. Technol.* **2024**, *58*, 14013–14021. [CrossRef]

19. Gautam, S.; Das, D.K.; Kaur, J.; Kumar, A.; Ubaidullah, M.; Hasan, M.; Yadav, K.K.; Gupta, R.K. Transition Metal-Based Nanoparticles as Potential Antimicrobial Agents: Recent Advancements, Mechanistic, Challenges, and Future Prospects. *Discov. Nano* **2023**, *18*, 84. [CrossRef]

20. Iyyappan, J.; Gaddala, B.; Gnanasekaran, R.; Gopinath, M.; Yuvaraj, D.; Kumar, V. Critical Review on Wastewater Treatment Using Photo Catalytic Advanced Oxidation Process: Role of Photocatalytic Materials, Reactor Design and Kinetics. *Case Stud. Chem. Environ. Eng.* **2024**, *9*, 100599. [CrossRef]

21. Wang, D.; Tian, H.; Zhu, J.; Lu, Z.; He, Z.; Song, S. Enhanced Photocatalytic Degradation of Toluene on Surface C- and CN-Modified TiO_2 Microspheres. *Appl. Surf. Sci.* **2024**, *673*, 160862. [CrossRef]

22. Nyabadza, A.; McCarthy, É.; Makhesana, M.; Heidarinassab, S.; Plouze, A.; Vazquez, M.; Brabazon, D. A Review of Physical, Chemical and Biological Synthesis Methods of Bimetallic Nanoparticles and Applications in Sensing, Water Treatment, Biomedicine, Catalysis and Hydrogen Storage. *Adv. Colloid Interface Sci.* **2023**, *321*, 103010. [CrossRef]

23. Álvarez-Chimal, R.; Ángel Arenas-Alatorre, J. Green Synthesis of Nanoparticles: A Biological Approach. In *Green Chemistry for Environmental Sustainability—Prevention-Assurance-Sustainability (P-A-S) Approach*; Shah, K., Ed.; IntechOpen: London, UK, 2023; ISBN 978-1-83769-389-4.

24. Ijaz, I.; Gilani, E.; Nazir, A.; Bukhari, A. Detail Review on Chemical, Physical and Green Synthesis, Classification, Characterizations and Applications of Nanoparticles. *Green Chem. Lett. Rev.* **2020**, *13*, 223–245. [CrossRef]

25. Sabry, B.A.; Badr, A.N.; Ahmed, K.A.; Desoukey, M.A.; Mohammed, D.M. Utilizing Lemon Peel Extract and Its Nano-Emulsion to Control Aflatoxin Toxicity in Rats. *Food Biosci.* **2022**, *50*, 101998. [CrossRef]

26. Gayathri Devi, K.; Clara Dhanemozhi, A.; Sathya Priya, L. Green Synthesis of Zinc Oxide Nanoparticles Using Lemon Extract for Waste Water Treatment. *Mater. Today Proc.* **2023**, *3*, S2214785323016425. [CrossRef]

27. Shubha, J.P.; Kavalli, K.; Adil, S.F.; Assal, M.E.; Hatshan, M.R.; Dubasi, N. Facile Green Synthesis of Semiconductive ZnO Nanoparticles for Photocatalytic Degradation of Dyes from the Textile Industry: A Kinetic Approach. *J. King Saud. Univ. Sci.* **2022**, *34*, 102047. [CrossRef]

28. Dhananjay, P.; Abhilash, M.R.; Shilpa, N.; Hemanth Kumar, N.K.; Gowtham, H.G.; Aiyaz, M.; Brijesh Singh, S.; Abdul, M.; Suhail, A.; Murali, M. Solar Irradiation Driven Catalytic Dye Degradation by Novel Biosynthesized Zinc Oxide Nanoparticles (ZnO–NPs) from Barleria Mysorensis: Kinetics, Reusability and Mineralization Studies. *J. Mol. Struct.* **2024**, *1303*, 137549. [CrossRef]

29. Barrios-Navarro, F.A.; Vilchis-Nestor, A.R.; Luque, P.A. Photocatalytic Degradation of Organic Dyes in Water Using Semiconductor ZnO Nanoparticles Synthesized Using Crataegus Mexicana Extract. *Mater. Chem. Phys.* **2024**, *318*, 129302. [CrossRef]

30. Assi, N.; Aberoomand Azar, P.; Saber Tehrani, M.; Waqif Husain, S.; Darwish, M.; Pourmand, S. Synthesis of ZnO-Nanoparticles by Microwave-Assisted Sol-Gel Method and Its Role in Photocatalytic Degradation of Food Dye Tartrazine (Acid Yellow 23). *Int. J. Nano Dimens.* **2014**, *8*, 3.

31. Algarni, T.S.; Al-Mohaimeed, A.M.; Abduh, N.A.Y.; Habab, R.A.; Alqahtani, S.M. Green Synthesis of Mixed $ZnO-SnO_2$ Nanoparticles for Solar-Assisted Degradation of Synthetic Dyes. *Catalysts* **2023**, *13*, 1509. [CrossRef]

32. John, D.M.; Pillai, N.S.; Sivan, A.; Lasya, P.; Archana, P.; Sreekanth, K.M.; Sivasubramanian, G.; Sreedhar, K.M. Ferromagnetic ZnO Nanostructures from an Organo Zinc Complex Formulated via Piper Longum L-Assisted Green Synthesis: Multifaceted Prospects in Photocatalysis, Antimicrobial Activity, and Cell Viability Studies. *Heliyon* **2024**, *10*, e33360. [CrossRef] [PubMed]

33. Lal, S.; Verma, R.; Chauhan, A.; Dhatwalia, J.; Guleria, I.; Ghotekar, S.; Thakur, S.; Mansi, K.; Kumar, R.; Kumari, A.; et al. Antioxidant, Antimicrobial, and Photocatalytic Activity of Green Synthesized ZnO-NPs from Myrica Esculenta Fruits Extract. *Inorg. Chem. Commun.* **2022**, *141*, 109518. [CrossRef]

34. George, J.M.; Aswani, M.T.; Kumar, M.V.P.; Varghese, B. Green Synthesis of ZnO Nanoparticles. In Proceedings of the International Conference on Science and Technology of Advanced Materials: STAM 20, Kothamangalam, India, 14–16 January 2020; p. 020001.

35. Negi, A.; Gangwar, R.; Kumar Vishwakarma, R.; Singh Negi, D. Antibacterial, Antioxidant and Photodegradation Potential of ZnO Nanoparticles Mediated via Roots of Taraxacum Officinale Radix. *Mater. Today Proc.* **2022**, *57*, 2435–2443. [CrossRef]

36. Omar, K.A.; Meena, B.I.; Muhammed, S.A. Study on the Activity of $ZnO-SnO_2$ Nanocomposite against Bacteria and Fungi. *Physicochem. Probl. Miner. Process.* **2016**, *52*, 945. [CrossRef]

37. Bakir, H.; Guvenc, U.; Kahraman, H.T.; Duman, S. Improved Lévy Flight Distribution Algorithm with FDB-Based Guiding Mechanism for AVR System Optimal Design. *Comput. Ind. Eng.* **2022**, *168*, 108032. [CrossRef]

38. Eswari, K.M.; Asaithambi, S.; Karuppaiah, M.; Sakthivel, P.; Balaji, V.; Ponelakkia, D.K.; Yuvakkumar, R.; Kumar, P.; Vijayaprabhu, N.; Ravi, G. Green Synthesis of ZnO Nanoparticles Using Abutilon Indicum and Tectona Grandis Leaf Extracts for Evaluation of Anti-Diabetic, Anti-Inflammatory and in-Vitro Cytotoxicity Activities. *Ceram. Int.* **2022**, *48*, 33624–33634. [CrossRef]

39. Alshehri, A.A.; Malik, M.A. Biogenic Fabrication of ZnO Nanoparticles Using Trigonella Foenum-Graecum (Fenugreek) for Proficient Photocatalytic Degradation of Methylene Blue under UV Irradiation. *J. Mater. Sci. Mater. Electron.* **2019**, *30*, 16156–16173. [CrossRef]

40. Aldeen, T.S.; Ahmed Mohamed, H.E.; Maaza, M. ZnO Nanoparticles Prepared via a Green Synthesis Approach: Physical Properties, Photocatalytic and Antibacterial Activity. *J. Phys. Chem. Solids* **2022**, *160*, 110313. [CrossRef]

41. Ameen, F.; Dawoud, T.; AlNadhari, S. Ecofriendly and Low-Cost Synthesis of ZnO Nanoparticles from Acremonium Potronii for the Photocatalytic Degradation of Azo Dyes. *Environ. Res.* **2021**, *202*, 111700. [CrossRef]

42. Mustafa, S.M.; Barzinjy, A.A.; Hamad, A.H.; Hamad, S.M. Green Synthesis of Ni Doped ZnO Nanoparticles Using Dandelion Leaf Extract and Its Solar Cell Applications. *Ceram. Int.* **2022**, *48*, 29257–29266. [CrossRef]

43. Nagaraj, K.; Naman, J.; Dixitkumar, M.; Priyanshi, J.; Thangamuniyandi, P.; Kamalesu, S.; Lokhandwala, S.; Parekh, N.M.; Rekha Panda, S.; Sakthinathan, S.; et al. Green Synthesis of Ag@ZnO Nanocomposites Using Cassia Alata Leaf Extract and Surfactant Complex for Photodegradation of Rhodamin6G. *Inorg. Chem. Commun.* **2023**, *151*, 110635. [CrossRef]

44. Song, Y.; Zhang, S.; Zhang, C.; Yang, Y.; Lv, K. Raman Spectra and Microstructure of Zinc Oxide Irradiated with Swift Heavy Ion. *Crystals* **2019**, *9*, 395. [CrossRef]

45. Volkov, V.V.; Oliver, D.J.; Perry, C.C. Polariton Condensation and Surface Enhanced Raman in Spherical ZnO Microcrystals. *Nat. Commun.* **2020**, *11*, 4908. [CrossRef] [PubMed]

46. Guo, S.; Du, Z.; Dai, S. Analysis of Raman Modes in Mn-doped ZnO Nanocrystals. *Phys. Status Solidi B* **2009**, *246*, 2329–2332. [CrossRef]

47. Konan, F.K.; Hartiti, B.; Batan, A.; Aka, B. X-Ray Diffraction, XPS, and Raman Spectroscopy of Coated ZnO:Al (1–7 At%) Nanoparticles. *E J. Surf. Sci. Nanotechnol.* **2019**, *17*, 163–168. [CrossRef]

48. Cui, S.; Wu, Y.; Cui, Z.; He, P.; Huang, N.; Xu, W.; Hu, J. Low-Frequency Ultrasound-Assisted Biosynthesis and Characterization of ZnO Nanoparticles Using Bacillus Thuringiensis against Tribolium Castaneum(Coleoptera, Tenebrionidae). *Mater. Lett.* **2023**, *341*, 134158. [CrossRef]

49. Bhosale, A.; Kadam, J.; Gade, T.; Sonawane, K.; Garadkar, K. Efficient Photodegradation of Methyl Orange and Bactericidal Activity of Ag Doped ZnO Nanoparticles. *J. Indian Chem. Soc.* **2023**, *100*, 100920. [CrossRef]

50. Pérez Velasco, E.A.; Betancourt Galindo, R.; Valdez Aguilar, L.A.; González Fuentes, J.A.; Puente Urbina, B.A.; Lozano Morales, S.A.; Sánchez Valdés, S. Effects of the Morphology, Surface Modification and Application Methods of ZnO-NPs on the Growth and Biomass of Tomato Plants. *Molecules* **2020**, *25*, 1282. [CrossRef]

51. Jowkar, Z.; Moaddeli, A.; Shafiei, F.; Tadayon, T.; Hamidi, S.A. Synthesis and Characterization of Mesoporous Zinc Oxide Nanoparticles and Evaluation of Their Biocompatibility in L929 Fibroblasts. *Clin. Exp. Dent. Res.* **2024**, *10*, e844. [CrossRef]

52. Ahmad, I.; Aslam, M.; Jabeen, U.; Zafar, M.N.; Malghani, M.N.K.; Alwadai, N.; Alshammari, F.H.; Almuslem, A.S.; Ullah, Z. ZnO and Ni-Doped ZnO Photocatalysts: Synthesis, Characterization and Improved Visible Light Driven Photocatalytic Degradation of Methylene Blue. *Inorganica Chim. Acta* **2022**, *543*, 121167. [CrossRef]

53. Mubeen, K.; Irshad, A.; Safeen, A.; Aziz, U.; Safeen, K.; Ghani, T.; Khan, K.; Ali, Z.; Ul Haq, I.; Shah, A. Band Structure Tuning of ZnO/CuO Composites for Enhanced Photocatalytic Activity. *J. Saudi Chem. Soc.* **2023**, *27*, 101639. [CrossRef]

54. Ghareib, M.; Abu Tahon, M.; Abdallah, W.E.; Hussein, M. Free Radical Scavenging Activity of Zinc Oxide Nanoparticles Biosynthesised Using *Aspergillus Carneus*. *Micro Nano Lett.* **2019**, *14*, 1157–1162. [CrossRef]

55. Kureshi, A.A.; Vaghela, H.M.; Kumar, S.; Singh, R.; Kumari, P. Green Synthesis of Gold Nanoparticles Mediated by Garcinia Fruits andTheir Biological Applications. *Pharm. Sci.* **2020**, *27*, 238–250. [CrossRef]

56. Shaghaghi, Z.; Mollaei, S.; Amani-Ghadim, A.R.; Abedini, Z. Green Synthesis of ZnO Nanoparticles Using the Aqueous Extract of Platanus Orientalis: Structural Characterization and Photocatalytic Activity. *Mater. Chem. Phys.* **2023**, *305*, 127900. [CrossRef]

57. Mallakpour, S.; Madani, M. Use of Silane Coupling Agent for Surface Modification of Zinc Oxide as Inorganic Filler and Preparation of Poly(Amide-Imide)/Zinc Oxide Nanocomposite Containing Phenylalanine Moieties. *Bull. Mater. Sci.* **2012**, *35*, 333–339. [CrossRef]

58. Rafique, S.; Bashir, S.; Akram, R.; Jawaid, S.; Bashir, M.; Aftab, A.; Attique, A.; Awan, S.U. In Vitro Anticancer Activity and Comparative Green Synthesis of ZnO/Ag Nanoparticles by Moringa Oleifera, Mentha Piperita, and Citrus Lemon. *Ceram. Int.* **2023**, *49*, 5613–5620. [CrossRef]

59. Mustafa, G.; Srivastava, S.; Kashif Aziz, M.; Kanaoujiya, R.; Rajkumar, C. Photosensitivity and Structural Properties of Vanadium-Doped ZnO and ZnO Nanoparticle at Various Calcined Temperature. *Mater. Today Proc.* **2023**, *8*, S2214785323046424. [CrossRef]

60. Malebadi, K.A.; Seheri, N.H.; Ojelere, O.; Onwudiwe, D.C. ZnO Nanoparticles Modified with G-C3N4: Optical and Structural Properties. *Mater. Sci. Eng. B* **2024**, *310*, 117676. [CrossRef]

61. Nath, M.R.; Ahmed, A.N.; Gafur, M.A.; Miah, M.Y.; Bhattacharjee, S. ZnO Nanoparticles Preparation from Spent Zinc–Carbon Dry Cell Batteries: Studies on Structural, Morphological and Optical Properties. *J. Asian Ceram. Soc.* **2018**, *6*, 262–270. [CrossRef]

62. Badawi, E.A.; Ibrahim, H.; Ebied, M.R.; Abdel-Rahman, M.; Khallaf, H.; Abdel Rahman, M.A. Study of the Optical Properties of Zno Nano-Structure at Different Ti Content. *Int. J. Thin Film. Sci. Technol.* **2022**, *11*, 257–266. [CrossRef]

63. Upadhyay, P.K.; Jain, V.K.; Sharma, K.; Sharma, R. Synthesis and Applications of ZnO Nanoparticles in Biomedicine. *Res. J. Pharm. Technol.* **2020**, *13*, 1636. [CrossRef]

64. Chen, R.; Zou, C.; Yan, X.; Gao, W. Zinc Oxide Nanostructures and Porous Films Produced by Oxidation of Zinc Precursors in Wet-Oxygen Atmosphere. *Prog. Nat. Sci. Mater. Int.* **2011**, *21*, 81–96. [CrossRef]

65. Perrotta, A.; Pilz, J.; Milella, A.; Coclite, A.M. Opto-Chemical Control through Thermal Treatment of Plasma Enhanced Atomic Layer Deposited ZnO: An in Situ Study. *Appl. Surf. Sci.* **2019**, *483*, 10–18. [CrossRef]

66. Sowmya, S.R.; Madhu, G.M.; Hashir, M. Studies on Nano-Engineered TiO_2 Photo Catalyst for Effective Degradation of Dye. *IOP Conf. Ser. Mater. Sci. Eng.* **2018**, *310*, 012026. [CrossRef]

67. Mohamed, A.; Yousef, S.; Nasser, W.S.; Osman, T.A.; Knebel, A.; Sánchez, E.P.V.; Hashem, T. Rapid Photocatalytic Degradation of Phenol from Water Using Composite Nanofibers under UV. *Environ. Sci. Eur.* **2020**, *32*, 160. [CrossRef]

68. Güell, F.; Galdámez-Martínez, A.; Martínez-Alanis, P.R.; Catto, A.C.; Da Silva, L.F.; Mastelaro, V.R.; Santana, G.; Dutt, A. ZnO-Based Nanomaterials Approach for Photocatalytic and Sensing Applications: Recent Progress and Trends. *Mater. Adv.* **2023**, *4*, 3685–3707. [CrossRef]

69. Jalali, N.; Rakhsha, A.; Nami, M.; Rashchi, F.; Mastelaro, V.R. Photocatalytic Activity and pH-Induced Morphological Changes of ZnO/CuO Nanocomposites Prepared by Chemical Bath Precipitation. *Energy Adv.* **2023**, *2*, 1051–1063. [CrossRef]

70. Nguyen, T.T.; Nam, S.-N.; Kim, J.; Oh, J. Photocatalytic Degradation of Dissolved Organic Matter under ZnO-Catalyzed Artificial Sunlight Irradiation System. *Sci. Rep.* **2020**, *10*, 13090. [CrossRef]

71. Ayu, D.G.; Gea, S.; Andriayani, D.J.; Telaumbanua, D.J.; Piliang, A.F.R.; Harahap, M.; Yen, Z.; Goei, R.; Tok, A.I.Y. Photocatalytic Degradation of Methylene Blue Using N-Doped ZnO/Carbon Dot (N-ZnO/CD) Nanocomposites Derived from Organic Soybean. *ACS Omega* **2023**, *8*, 14965–14984. [CrossRef]

72. Rajamanickam, D.; Shanthi, M. Photocatalytic Degradation of an Organic Pollutant by Zinc Oxide—Solar Process. *Arab. J. Chem.* **2016**, *9*, S1858–S1868. [CrossRef]

73. Reza, K.M.; Kurny, A.; Gulshan, F. Parameters Affecting the Photocatalytic Degradation of Dyes Using TiO$_2$: A Review. *Appl. Water Sci.* **2017**, *7*, 1569–1578. [CrossRef]

74. Jida, S.M.; Zerefa, E.A. Preparation and Photocatalysis of ZnO/Bentonite Based on Adsorption and Photocatalytic Activity. *Mater. Res. Express* **2023**, *10*, 035502. [CrossRef]

75. Gul, T.; Khan, I.; Ahmad, B.; Ahmad, S.; Alsaiari, A.A.; Almehmadi, M.; Abdulaziz, O.; Alsharif, A.; Khan, I.; Saeed, K. Efficient Photodegradation of Methyl Red Dye by Kaolin Clay Supported Zinc Oxide Nanoparticles with Their Antibacterial and Antioxidant Activities. *Heliyon* **2023**, *9*, e16738. [CrossRef]

76. Saeed, M.; Akram, N.; Atta-ul-Haq; Naqvi, S.A.R.; Usman, M.; Abbas, M.A.; Adeel, M.; Nisar, A. Green and Eco-Friendly Synthesis of Co$_3$O$_4$ and Ag-Co$_3$O$_4$: Characterization and Photo-Catalytic Activity. *Green Process. Synth.* **2019**, *8*, 382–390. [CrossRef]

77. Magar, M.H.; Adole, V.A.; Waghchaure, R.H.; Pawar, T.B. Efficient Photocatalytic Degradation of Eosin Blue Dye and Antibacterial Study Using Nanostructured Zinc Oxide and Nickel Modified Zinc Oxide. *Results Chem.* **2022**, *4*, 100537. [CrossRef]

78. Xu, Z.; Zada, N.; Habib, F.; Ullah, H.; Hussain, K.; Ullah, N.; Bibi, M.; Bibi, M.; Ghani, H.; Khan, S.; et al. Enhanced Photocatalytic Degradation of Malachite Green Dye Using Silver–Manganese Oxide Nanoparticles. *Molecules* **2023**, *28*, 6241. [CrossRef]

79. Tran, H.D.; Nguyen, D.Q.; Do, P.T.; Tran, U.N.P. Kinetics of Photocatalytic Degradation of Organic Compounds: A Mini-Review and New Approach. *RSC Adv.* **2023**, *13*, 16915–16925. [CrossRef]

80. Zhan, X.; Yan, C.; Zhang, Y.; Rinke, G.; Rabsch, G.; Klumpp, M.; Schäfer, A.I.; Dittmeyer, R. Investigation of the Reaction Kinetics of Photocatalytic Pollutant Degradation under Defined Conditions with Inkjet-Printed TiO$_2$ Films—From Batch to a Novel Continuous-Flow Microreactor. *React. Chem. Eng.* **2020**, *5*, 1658–1670. [CrossRef]

81. Nasrallah, N.; Kebir, M.; Koudri, Z.; Trari, M. Photocatalytic Reduction of Cr(VI) on the Novel Hetero-System CuFe$_2$O$_4$/CdS. *J. Hazard. Mater.* **2011**, *185*, 1398–1404. [CrossRef] [PubMed]

82. Rini, N.P.; Istiqomah, N.I.; Sunarta; Suharyadi, E. Enhancing Photodegradation of Methylene Blue and Reusability Using CoO/ZnO Composite Nanoparticles. *Case Stud. Chem. Environ. Eng.* **2023**, *7*, 100301. [CrossRef]

83. Fernández, A.; Lassaletta, G.; Jiménez, V.M.; Justo, A.; González-Elipe, A.R.; Herrmann, J.-M.; Tahiri, H.; Ait-Ichou, Y. Preparation and Characterization of TiO$_2$ Photocatalysts Supported on Various Rigid Supports (Glass, Quartz and Stainless Steel, Comparative Studies of Photocatalytic Activity in Water Purification. *Appl. Catal. B Environ.* **1995**, *7*, 49–63. [CrossRef]

84. Uribe-López, M.C.; Hidalgo-López, M.C.; López-González, R.; Frías-Márquez, D.M.; Núñez-Nogueira, G.; Hernández-Castillo, D.; Alvarez-Lemus, M.A. Photocatalytic Activity of ZnO Nanoparticles and the Role of the Synthesis Method on Their Physical and Chemical Properties. *J. Photochem. Photobiol. A Chem.* **2021**, *404*, 112866. [CrossRef]

85. Zambrano, J.; García-Encina, P.A.; Jiménez, J.J.; López-Serna, R.; Irusta-Mata, R. Photolytic and Photocatalytic Removal of a Mixture of Four Veterinary Antibiotics. *J. Water Process. Eng.* **2022**, *48*, 102841. [CrossRef]

86. Rehana, D.; Mahendiran, D.; Kumar, R.S.; Rahiman, A.K. In Vitro Antioxidant and Antidiabetic Activities of Zinc Oxide Nanoparticles Synthesized Using Different Plant Extracts. *Bioprocess. Biosyst. Eng.* **2017**, *40*, 943–957. [CrossRef] [PubMed]

87. Shabbir Awan, S.; Taj Khan, R.; Mehmood, A.; Hafeez, M.; Rizwan Abass, S.; Nazir, M.; Raffi, M. Ailanthus Altissima Leaf Extract Mediated Green Production of Zinc Oxide (ZnO) Nanoparticles for Antibacterial and Antioxidant Activity. *Saudi J. Biol. Sci.* **2023**, *30*, 103487. [CrossRef] [PubMed]

88. Ahmad, N.; Ali, S.; Abbas, M.; Fazal, H.; Saqib, S.; Ali, A.; Ullah, Z.; Zaman, S.; Sawati, L.; Zada, A.; et al. Antimicrobial Efficacy of Mentha Piperata-Derived Biogenic Zinc Oxide Nanoparticles against UTI-Resistant Pathogens. *Sci. Rep.* **2023**, *13*, 14972. [CrossRef]

89. Batool, S.; Hasan, M.; Dilshad, M.; Zafar, A.; Tariq, T.; Wu, Z.; Chen, R.; Gul Hassan, S.; Munawar, T.; Iqbal, F.; et al. Green Synthesis of Cordia Myxa Incubated ZnO, Fe$_2$O$_3$, and Co$_3$O$_4$ Nanoparticle: Characterization, and Their Response as Biological and Photocatalytic Agent. *Adv. Powder Technol.* **2022**, *33*, 103780. [CrossRef]

90. Arumugam, V.; Subramaniam, S.; Krishnan, V. Green Synthesis and Characterization of Zinc Oxide Nanoparticles Using Berberis Tinctoria Lesch. leaves and fruits extract of multi-biological applications. *Nanomed. Res. J.* **2021**, *6*, 128–147. [CrossRef]

91. Yagoub, A.E.A.; Al-Shammari, G.M.; Al-Harbi, L.N.; Subash-Babu, P.; Elsayim, R.; Mohammed, M.A.; Yahya, M.A.; Fattiny, S.Z.A. Antimicrobial Properties of Zinc Oxide Nanoparticles Synthesized from Lavandula Pubescens Shoot Methanol Extract. *Appl. Sci.* **2022**, *12*, 11613. [CrossRef]

92. Mahmure, Ü.Ö.; Özgür, D.; Melda, A.Y. Investigation of Antibacterial and Photo Catalytic Efficiency of Green ZnO Nanoparticles That Synthesized with Celosia Cristata Flower Extract. *Turk. J. Chem.* **2021**, *46*, 59–85. [CrossRef]

93. Umavathi, S.; Mahboob, S.; Govindarajan, M.; Al-Ghanim, K.A.; Ahmed, Z.; Virik, P.; Al-Mulhm, N.; Subash, M.; Gopinath, K.; Kavitha, C. Green Synthesis of ZnO Nanoparticles for Antimicrobial and Vegetative Growth Applications: A Novel Approach for Advancing Efficient High Quality Health Care to Human Wellbeing. *Saudi J. Biol. Sci.* **2021**, *28*, 1808–1815. [CrossRef] [PubMed]

94. Jiang, Y.; Zhang, L.; Wen, D.; Ding, Y. Role of Physical and Chemical Interactions in the Antibacterial Behavior of ZnO Nanoparticles against E. *Coli. Mater. Sci. Eng. C* **2016**, *69*, 1361–1366. [CrossRef] [PubMed]

95. Fahmy, B.; Cormier, S.A. Copper Oxide Nanoparticles Induce Oxidative Stress and Cytotoxicity in Airway Epithelial Cells. *Toxicol. Vitr.* **2009**, *23*, 1365–1371. [CrossRef]

96. Li, D.; Ding, Z.; Du, K.; Ye, X.; Cheng, S. Reactive Oxygen Species as a Link between Antioxidant Pathways and Autophagy. *Oxid. Med. Cell. Longev.* **2021**, *2021*, 1–11. [CrossRef]

97. Ong, K.S.; Cheow, Y.L.; Lee, S.M. The Role of Reactive Oxygen Species in the Antimicrobial Activity of Pyochelin. *J. Adv. Res.* **2017**, *8*, 393–398. [CrossRef] [PubMed]

98. Syed-Ab-Rahman, S.F.; Arkhipov, A.; Wass, T.J.; Xiao, Y.; Carvalhais, L.C.; Schenk, P.M. Rhizosphere Bacteria Induce Programmed Cell Death Defence Genes and Signalling in Chilli Pepper. *J. Appl. Microbiol.* **2022**, *132*, 3111–3124. [CrossRef]

99. Brayner, R.; Ferrari-Iliou, R.; Brivois, N.; Djediat, S.; Benedetti, M.F.; Fiévet, F. Toxicological Impact Studies Based on *Escherichia Coli* Bacteria in Ultrafine ZnO Nanoparticles Colloidal Medium. *Nano Lett.* **2006**, *6*, 866–870. [CrossRef]

100. Kumar, A.; Pandey, A.K.; Singh, S.S.; Shanker, R.; Dhawan, A. Cellular Uptake and Mutagenic Potential of Metal Oxide Nanoparticles in Bacterial Cells. *Chemosphere* **2011**, *83*, 1124–1132. [CrossRef]

101. Singh, R.; Cheng, S.; Singh, S. Oxidative Stress-Mediated Genotoxic Effect of Zinc Oxide Nanoparticles on Deinococcus Radiodurans. *3 Biotech.* **2020**, *10*, 66. [CrossRef]

102. Kumar, A.; Pandey, A.K.; Singh, S.S.; Shanker, R.; Dhawan, A. Engineered ZnO and TiO_2 Nanoparticles Induce Oxidative Stress and DNA Damage Leading to Reduced Viability of Escherichia Coli. *Free Radic. Biol. Med.* **2011**, *51*, 1872–1881. [CrossRef]

103. Jones, R.M.; Wu, H.; Wentworth, C.; Luo, L.; Collier-Hyams, L.; Neish, A.S. Salmonella AvrA Coordinates Suppression of Host Immune and Apoptotic Defenses via JNK Pathway Blockade. *Cell Host Microbe* **2008**, *3*, 233–244. [CrossRef] [PubMed]

104. Ghosh, A.; Stuehr, D.J. Soluble Guanylyl Cyclase Requires Heat Shock Protein 90 for Heme Insertion during Maturation of the NO-Active Enzyme. *Proc. Natl. Acad. Sci. USA* **2012**, *109*, 12998–13003. [CrossRef] [PubMed]

105. Tahraoui, H.; Belhadj, A.-E.; Hamitouche, A.-E. Prediction of the Bicarbonate Amount in Drinking Water in the Region of Médéa Using Artificial Neural Network Modelling. *Kem. U Ind. Časopis Kemičara Kem. Inženjera Hrvat.* **2020**, *69*, 595–602. [CrossRef]

106. Tahraoui, H.; Belhadj, A.-E.; Moula, N.; Bouranene, S.; Amrane, A. Optimisation and Prediction of the Coagulant Dose for the Elimination of Organic Micropollutants Based on Turbidity. *Kem. U Ind.* **2021**, *70*, 675–691. [CrossRef]

107. Khan, A.U.R.; Khan, S.U.R.; Al-Mohaimeed, A.M.; Al-onazi, W.A.; Chen, T.-W.; Imran, M. Green Mediated Approach to Investigate the Optical, Structural, Photocatalytic, Magnetic and Dielectric Properties of Cr^{3+} Doped ZnO Nanoparticles for Energy Applications. *Ceram. Int.* **2024**, *50*, 42809–42817. [CrossRef]

108. Goudjil, M.B.; Zighmi, S.; Hamada, D.; Mahcene, Z.; Bencheikh, S.E.; Ladjel, S. Biological Activities of Essential Oils Extracted from Thymus Capitatus (Lamiaceae). *South Afr. J. Bot.* **2020**, *128*, 274–282. [CrossRef]

109. Mousavi-Khattat, M.; Keyhanfar, M.; Razmjou, A. A Comparative Study of Stability, Antioxidant, DNA Cleavage and Antibacterial Activities of Green and Chemically Synthesized Silver Nanoparticles. *Artif. Cells Nanomed. Biotechnol.* **2018**, *46*, 1022–1031. [CrossRef]

110. Islam, M.F.; Islam, S.; Miah, M.A.S.; Huq, A.K.O.; Saha, A.K.; Mou, Z.J.; Mondol, M.M.H.; Bhuiyan, M.N.I. Green Synthesis of Zinc Oxide Nano Particles Using *Allium Cepa* L. Waste Peel Extracts and Its Antioxidant and Antibacterial Activities. *Heliyon* **2024**, *10*, e25430. [CrossRef]

111. Tahraoui, H.; Belhadj, A.-E.; Triki, Z.; Boudellal, N.R.; Seder, S.; Amrane, A.; Zhang, J.; Moula, N.; Tifoura, A.; Ferhat, R. Mixed Coagulant-Flocculant Optimization for Pharmaceutical Effluent Pretreatment Using Response Surface Methodology and Gaussian Process Regression. *Process Saf. Environ. Prot.* **2023**, *169*, 909–927. [CrossRef]

112. Tahraoui, H.; Belhadj, A.-E.; Amrane, A.; Houssein, E.H. Predicting the Concentration of Sulfate Using Machine Learning Methods. *Earth Sci. Inform.* **2022**, *15*, 1–22. [CrossRef]

113. Bouchelkia, N.; Tahraoui, H.; Amrane, A.; Belkacemi, H.; Bollinger, J.-C.; Bouzaza, A.; Zoukel, A.; Zhang, J.; Mouni, L. Jujube Stones Based Highly Efficient Activated Carbon for Methylene Blue Adsorption: Kinetics and Isotherms Modeling, Thermodynamics and Mechanism Study, Optimization via Response Surface Methodology and Machine Learning Approaches. *Process Saf. Environ. Prot.* **2023**, *170*, 513–535. [CrossRef]

114. Mechati, S.; Zamouche, M.; Tahraoui, H.; Filali, O.; Mazouz, S.; Bouledjemer, I.N.E.; Toumi, S.; Triki, Z.; Amrane, A.; Kebir, M. Modeling and Optimization of Hybrid Fenton and Ultrasound Process for Crystal Violet Degradation Using AI Techniques. *Water* **2023**, *15*, 4274. [CrossRef]

115. Smara, M.; Khalladi, R.; Moulai-Mostefa, N.; Madi, K.; Mansour, D.; Lekmine, S.; Benslama, O.; Tahraoui, H.; Zhang, J.; Amrane, A. Efficiency of Hydrogen Peroxide and Fenton Reagent for Polycyclic Aromatic Hydrocarbon Degradation in Contaminated Soil: Insights from Experimental and Predictive Modeling. *Processes* **2024**, *12*, 621. [CrossRef]

116. Hamri, N.; Imessaoudene, A.; Hadadi, A.; Cheikh, S.; Boukerroui, A.; Bollinger, J.-C.; Amrane, A.; Tahraoui, H.; Tran, H.N.; Ezzat, A.O. Enhanced Adsorption Capacity of Methylene Blue Dye onto Kaolin through Acid Treatment: Batch Adsorption and Machine Learning Studies. *Water* **2024**, *16*, 243. [CrossRef]

117. Nedjhioui, M.; Nasrallah, N.; Kebir, M.; Tahraoui, H.; Bouallouche, R.; Assadi, A.A.; Amrane, A.; Jaouadi, B.; Zhang, J.; Mouni, L. Designing an Efficient Surfactant–Polymer–Oil–Electrolyte System: A Multi-Objective Optimization Study. *Processes* **2023**, *11*, 1314. [CrossRef]

118. Tahraoui, H.; Amrane, A.; Belhadj, A.-E.; Zhang, J. Modeling the Organic Matter of Water Using the Decision Tree Coupled with Bootstrap Aggregated and Least-Squares Boosting. *Environ. Technol. Innov.* **2022**, *27*, 102419. [CrossRef]

119. Kebir, M.; Benramdhan, I.-K.; Nasrallah, N.; Tahraoui, H.; Bait, N.; Benaissa, H.; Ameraoui, R.; Zhang, J.; Assadi, A.A.; Mouni, L. Surface Response Modeling of Homogeneous Photo Fenton Fe (III) and Fe (II) Complex for Sunlight Degradation and Mineralization of Food Dye. *Catal. Commun.* **2023**, *183*, 106780. [CrossRef]

120. Yahoum, M.M.; Toumi, S.; Hentabli, S.; Tahraoui, H.; Lefnaoui, S.; Hadjsadok, A.; Amrane, A.; Kebir, M.; Moula, N.; Assadi, A.A. Experimental Analysis and Neural Network Modeling of the Rheological Behavior of Xanthan Gum and Its Derivatives. *Materials* **2023**, *16*, 2565. [CrossRef] [PubMed]

121. Zamouche, M.; Tahraoui, H.; Laggoun, Z.; Mechati, S.; Chemchmi, R.; Kanjal, M.I.; Amrane, A.; Hadadi, A.; Mouni, L. Optimization and Prediction of Stability of Emulsified Liquid Membrane (ELM): Artificial Neural Network. *Processes* **2023**, *11*, 364. [CrossRef]

122. Zamouche, M.; Chermat, M.; Kermiche, Z.; Tahraoui, H.; Kebir, M.; Bollinger, J.-C.; Amrane, A.; Mouni, L. Predictive Model Based on K-Nearest Neighbor Coupled with the Gray Wolf Optimizer Algorithm (KNN_GWO) for Estimating the Amount of Phenol Adsorption on Powdered Activated Carbon. *Water* **2023**, *15*, 493. [CrossRef]

123. Tahraoui, H.; Belhadj, A.-E.; Hamitouche, A.; Bouhedda, M.; Amrane, A. Predicting the Concentration of Sulfate (So_4^{2-}) in Drinking Water Using Artificial Neural Networks: A Case Study: Médéa-Algeria. *Desalination Water Treat.* **2021**, *217*, 181–194. [CrossRef]

124. Hadadi, A.; Imessaoudene, A.; Bollinger, J.-C.; Bouzaza, A.; Amrane, A.; Tahraoui, H.; Mouni, L. Aleppo Pine Seeds (*Pinus halepensis* Mill.) as a Promising Novel Green Coagulant for the Removal of Congo Red Dye: Optimization via Machine Learning Algorithm. *J. Environ. Manag.* **2023**, *331*, 117286. [CrossRef] [PubMed]

125. Tahraoui, H.; Toumi, S.; Hassein-Bey, A.H.; Bousselma, A.; Sid, A.N.E.H.; Belhadj, A.-E.; Triki, Z.; Kebir, M.; Amrane, A.; Zhang, J. Advancing Water Quality Research: K-Nearest Neighbor Coupled with the Improved Grey Wolf Optimizer Algorithm Model Unveils New Possibilities for Dry Residue Prediction. *Water* **2023**, *15*, 2631. [CrossRef]